Babeş-Bolyai University

Faculty of Physics

Raluca-Andreea Luchian

Experimental and computational spectroscopy applied to antiepileptic and anticancer drugs

PhD Thesis Summary

Supervisor

Prof.dr. Vasile Chiş

Cluj-Napoca
2018

Keywords

Active pharmaceutical ingredients

Antiepileptic

Anticancer

Spectroscopy

DFT

Levetiracetam

Diphenylhydantoin

Imatinib

Acknowledgments

I would like to thank my supervisor, Prof. dr. Vasile Chiş for allowing me to join his group and to enter the fascinating world of research, for his encouragement, patient guidance and advices he has provided during my time as a PhD student.

Completing this work would not have been possible without the support and friendship provided by the other members in the group of prof. Chiş and from the Department of Biomolecular Physics, Babeş-Bolyai University. Many thanks to Dr. Nicolae Leopold for guiding me during the UV-Vis and Raman measurements in the SETA and Raman-SPM laboratory. Dr. Mihai Vasilescu is acknowledged for NMR measurements on LEV and IMT and dr. Dana Maniu for the last minute Raman images on tablet samples.

Special thanks to Dr. Major Zoltan from the University of Medicine and Pharmacy Iuliu Haţieganu, Cluj-Napoca, for providing the LEV drug samples.

I would like to express particular thanks to dr. Mircea Oltean, the post-doc in the group of prof. Chiş, for guiding me with the quantum chemical calculations. His advice and support was always there when I needed it most.

I would also like to thank my lab mates, dr. Alexandra Falamas, drd. Istvan Toth and drd. Reka Domomkos, for making my experience in the lab exciting and fun.

Last, but not least I would like to thank my family for all their love and encouragement. Thank you very much!

The research undertaken for this thesis was conducted using the Babeş-Bolyai University Research infrastructure financed by the Romanian Government through the program PN II – Capacities – project title Integrated Network for Interdisciplinary Research – INIR and the project MADECIP (POSCEE COD SMIS CSNR 48801/1862).

List of publications during PhD thesis work

Raluca Luchian, Emil Vinţeler, Cosmina Chiş, Mihai Vasilescu, Nicolae Leopold, João P. Prates Ramalho, Vasile Chiş, ''Conformational preference and spectroscopical characteristics of the active pharmaceutical ingredient Levetiracetam'', *Journal of Pharmaceutical Sciences*, 106 (2017) 3564-3573, DOI: 10.1016/j.xphs.2017.08.008.

Raluca Luchian, Emil Vinţeler, Cosmina Chiş, Mihai Vasilescu, Nicolae Leopold, Vasile Chiş, ''Molecular structure of phenytoin: NMR, UV-Vis and quantum chemical calculations'', *Croatica Chemica Acta*, 88 (2015) 511-522, DOI: 10.5562/cca2767.

Emil Vinţeler, Nicoleta-Florina Stan, **Raluca Luchian**, Călin Căinap, Joao P. Prates-Ramalho, Vasile Chis, ''Conformational landscape and low lying excited states of imatinib'', *Journal of Molecular Modeling*, 21 (2015) 84, DOI: 10.1007/s00894-015-2639-8.

Raluca Luchian, Réka-Anita Domokos, Cosmina Chiş, Mihai Vasilescu, Emil Vinţeler, Vasile Chiş, "Methods and models for calculating NMR spectra: Levetiracetam as a test case", Studia UBB Physica, 59 (LIX), 2 (2014) 85-98.

Table of contents

Introduction

Physical and chemical properties of the active pharmaceutical ingredients (APIs) are greatly influenced by the arrangement of molecules in the crystal, which in turn, is determined by the conformational space of the component molecules [Dat04]. Thus, the API's structure as well as its molecular environment plays a dominant role on the drug's physicochemical properties like: solubility, dissolution rate, stability, absorption, hygroscopicity and bioavailability. For these reasons, it is clear that understanding the relationships between physical structures and the properties of a particular API is crucial for its development into a drug product.

An important issue related to the pharmaceutical industry is the medicines counterfeiting, both for brand and generic products [Deg14, Ora15]. The risks associated with the replacement of brand drugs by generic substitutions are important, due to the fact that the latter could manifest bioequivalence, therapy and adverse effects issues [Kra07, Bia10, Vai15, Ati16].

Spectroscopic characterization of APIs is of utmost importance for the pharmaceutical industry. Various methods of experimental and computational spectroscopy are synergistically applied nowadays for their structure determination, as well as for revealing subtle transformations between their solid and liquid phases [Pin17, Hig17, Buc17]. The combination of experimental and computational (quantum chemical) methods can bring new and useful information on the geometric and electronic structure of APIs. Considering the above mentioned issues, during the research performed for this PhD thesis we aimed to get new insights into the structure and electronic properties of a series of APIs used for producing antiepileptic and anticancer drugs. For this purpose, we correlated the results obtained by using experimental (Raman, IR, UV-Vis, NMR) and computational techniques.

The thesis is divided into two main parts. The first part includes this introductory chapter as well as another two chapters. In the first chapter we give a general overview of density functional theory (DFT).

The second chapter of the thesis gives the experimental and computational details valid for all the investigated compounds. Particular details for each compound will also be included in the corresponding section of the dedicated chapter.

The second part of the thesis contains three chapters, one for each of the three investigated APIs.

In chapter 3 we focused on the analysis of the possible conformers and the conformational change between solid and liquid states of levetiracetam (LEV) in gas phase as well as in water and ethanol, aiming to describe the 3D structure and energetic stability of its conformers, in order to achieve a better understanding of its pharmacodynamics.

Our first aim was to describe the differences between the known solid state geometries of LEV and its liquid (and gas-) phase structures.

The experimental UV-Vis and NMR spectra of LEV have been explained on the basis of the contributions due to monomers as well as Boltzmann weighted contributions of the dimers. The most intense electronic excitations are dominantly driven by intramolecular charge-transfer type transitions, from oxopyrrolidin to amide unit for monomer and from the butanamide groups to the carbonyl units in the oxopyrrolidin rings in case of dimer [Luc17].

Both, ^{1}H and ^{13}C NMR spectra of LEV have been reliably assigned based on theoretical data and our results suggest that the formation of dimeric structures is evident at the working concentration used for recording the NMR spectra [Luc14].

Moreover, for this compound we were interested to check the potential of Raman spectroscopy for discriminating between the different formulations of a particular manufacturer as well as between several manufacturers of the same formulation of LEV.

Chapter 4 presents a joint experimental and computational investigation on diphenylhydantoin (DPH), which is the oldest non-sedative antiepileptic drug indicated for the treatment of epilepsy. Despite being extensively used as an active pharmaceutical ingredient its "biological face" [Tie08] still remains incompletely elucidated. Due to the presence of the carbonyl and imide groups in its structure, the possibility for this compound to be involved in hydrogen bonding intermolecular interactions is obvious. Consequently we studied the dimerization process of DPH through hydrogen bonding interactions by using quantum chemical calculations. Moreover, combining the experimental UV-Vis and NMR techniques with quantum chemical calculations we addressed the effect of such hydrogen bonding interactions on the electronic transitions as well as on the NMR chemical shifts of DPH [Luc15].

In chapter five we investigated the anticancer drug Imatinib (IMT), which is a first generation tyrosine-kinase inhibitor (TKI), mainly used in the treatment of chronic myelogenous leukemia and gastrointestinal stromal tumors. This API acts selectively on Abl tyrosine kinases Mast/stem cell growth factor receptor (c-Kit) and platelet-derived growth factor receptors.

For clarifying its mechanism of action, the accurate description of the 3D arrangement and molecular properties of thermally accessible conformational states is crucial.

This is why we were interested in the possible conformers of IMT and their energetic orders and we were able to identified twenty unique conformers of IMT in water in a relative Gibbs energy window of 1.69 kcal·mol^{-1}. Subsequently, the most stable nine structures, whose relative energies are within the room temperature energy, were employed to compute the electronic excitation energies, which in turn were used to explain the experimental observations.

UV-Vis study was conducted to check if the theoretically identified most stable conformers can explain the experimental observations. A reliable assignment of experimental electronic absorption data is highly needed, which, in this study is given in terms of IMT monomeric structures [Vin15].

Chapter 1

DFT METHODS USED TO CALCULATE THE ELECTRONIC STRUCTURE OF MOLECULES

The advantages of density functional theory (DFT) computational methodology rely on one hand, on the greater accuracy of the provided theoretical results, but also on the lower computational resources required for the calculations on averaged and large sized molecules. Due to the huge impact of the DFT computational results in spectroscopy, the "computational spectroscopy" field has been recognized in the scientific literature in the last 10 years [Bar15].

1.1 Basics of DFT

The (molecular) modern version of DFT has been developed by Hohenberg, Kohn and Sham and it is based on the two Hohenberg-Kohn theorems [Hoh64].

The first Hohenberg-Kohn theorem represents a proof of principle, while the second one gives the variational principle for obtaining the electron density in a variational way. It provides the proof that the electronic density uniquely determines the Hamilton operator and thus all properties of the system.

In the framework of DFT, the expression of the energy is separated into those parts that depend on the actual system, i.e., the potential energy due to the nuclei-electron attraction and those which are universal in the sense that their form is independent of N, R_α and Z_α:

$$E_0[\rho_0] = \underbrace{\int \rho_0(\vec{r}) V_{ne} d\vec{r}}_{system\ dependent} + \underbrace{T[\rho_0] + E_{ee}[\rho_0]}_{universally\ valid} \quad (1.1.7)$$

The last two system independent terms form the Hohenberg-Kohn functional $F_{HK}[\rho_0]$:

$$F_{HK}[\rho] = T[\rho] + E_{ee}[\rho] = \langle \Psi | \hat{T} + \widehat{V_{ee}} | \Psi \rangle \quad (1.1.8)$$

$F_{HK}[\rho]$ contains the functional for the kinetic energy $T[\rho]$ and that for the electron-electron interaction, $E_{ee}[\rho]$. Finding explicit expressions for the yet unknown functionals $T[\rho]$ and $E_{ncl}[\rho]$ represents the major challenge in Density Functional Theory.

Kohn and Sham (KS) introduced the concept of a fictitious non-interacting reference system (free electron system) built from a set of orbitals such that the major part of the kinetic energy can be computed to good accuracy [KS65]. The remainder part of the kinetic energy was included in the non-classical contributions to the electron-electron repulsion – which are also unknown, but usually fairly small.

The idea of Kohn and Sham was that for every system of interacting electrons in an external potential υ(r) there is a corresponding system without interaction, which translates into the existence of a local potential $\upsilon_S(r)$ so that the system of non-interacting electrons within this potential will yield exactly the same electron density as the real one. Assuming such a potential, one can compute the corresponding Kohn-Sham orbitals and the exact electron density based on the equations:

$$\hat{H}_S = \sum_i \hat{h}_S(i) = \sum_i (-\frac{1}{2}\nabla_i^2 + \upsilon_S(r_i)) \quad (1.1.12)$$

$$\hat{h}_S(1)\Phi_i(1) = \varepsilon_i(1)\Phi_i(1) \quad (1.1.13)$$

$$\Psi_S = |\Phi_1(1)\Phi_2(2) \dots \Phi_N(N) > \quad (1.1.14)$$

$$\rho_S(r) = \sum_{i=1}^{N} \sum_S |\Phi_i(r,s)|^2 = \rho_{exact}(r) \quad (1.1.15)$$

The exact kinetic energy of the non-interacting reference system with the same density as the real can be obtained using atomic orbitals with the relation:

$$T_{KS} = -\frac{1}{2}\sum_{i=1}^{N} \langle \Psi_i | \nabla^2 | \Psi_i \rangle \quad (1.1.17)$$

and in the the KS formulation, the kinetic energy can be written as:

$$T[\rho] = T_{KS} + (T - T_{KS}) \quad (1.1.19)$$

with the functional F[ρ] written as:

$$F[\rho] = T_{KS}[\rho] + J[\rho] + E_{XC}[\rho] \quad (1.1.20)$$

This so-called exchange-correlation functional (E_{XC}) contains the Coulomb repulsion between electrons, the non-classical exchange and correlation effects, but also a portion that represents the correction to the kinetic energy.

The general approach for obtaining the energy of the fundamental state can be summarized as follows: first, a trial density is chosen to start with, which allows the determination of the effective potential using an adequate form for the correlation-exchange functional. A new density is then found by solving the Kohn-Sham equations and compared to the previous density. If the two are equal, the ground state energy can be found, otherwise the iterative process is resumed.

The electronic energy in the KS approach can be written as:

$$E = T_S[\rho] + \int \upsilon(r)\rho(r)dr + \frac{1}{2}\int \frac{\rho(r)\rho(r')}{|r-r'|} dr dr' + E_{XC}[\rho] \quad (1.1.24)$$

The early implementation of DFT is the local density-functional approximation (LDA), which is derived from the case of a homogeneous electron gas. Lately, generalized gradient approximation (GGA) corrections were developed and have been shown to improve the calculated results, especially for molecular bond energies and electronic

spectra. Further progress in DFT is brought by the hybrid xc functionals which include a fraction of the HF exchange.

New approximate xc functionals (meta-GGA type) have recently been developed by including the electron kinetic energy density and the Laplacian of the electron density.

The approximations with the widest spread in use for the exchange-correlation energy and which have given the best results are the hybrid functionals. The best known functional of this type and widely applied for molecular structures and properties calculations is B3LYP – a hybrid exchange-correlation functional with 3 parameters which uses the correlation functional of Lee, Yang and Parr (LYP) [Bec93, Lee88, Vos80, Ste94]:

$$E_{xc}^{B3LYP} = aE_{xc}^{Slater} + (a-1)E_{xc}^{LDA} + bE_c^B + (1-c)E_c^{LDA} \qquad (1.3.37)$$

where a=0.20; b=0.72 and c=0.81

Its success is due to the high accuracy theoretical results it provides for a wide range of molecular properties like: geometries, dipole moments, polarizabilities, IR, Raman, RES, RMN or UV-Vis spectra, ionization potentials, electrostatic molecular potentials, etc.

Another well-known example of a hybrid functional, particularly successful in predicting the electronic transitions in molecule is PBE0 [Ada99]. No fitting parameters were used and the percentage of exact exchange is fixed at 25% [Per96, Per97].

Over time, many reviews on DFT focused on a variety of aspects including the theory, methodological developments, and the practical application of DFT to specific problems. The review of Sousa *et al.* [Sou07] gives an accurate account of the current status of the field. Thus, the essential type of density functionals can be arranged as the rungs on a ladder (Jacob's ladder of DFT [Mat02]) and they are based on LDA, GGA, meta-GGA, hybrid DF, hybrid-meta GGA and fully non-local approaches.

1.2 Basis sets for *ab initio* and DFT calculations

One of the approximations inherent in all *ab-initio* methods for quantum chemistry is the introduction of a basis set, which is a set of known functions used to construct the molecular orbitals. If the basis functions are $\varphi_1, \varphi_2, \ldots, \varphi_N$ then an individual molecular orbital is written:

$$\Phi_i = \sum_{\mu=1}^{K} c_{\mu i}\varphi_\mu \qquad (1.2.1)$$

where $c_{\mu i}$ are the expansion coefficients of the molecular orbital.

The problem of finding the molecular orbitals is reduced to finding a set of coefficients for each of the orbitals. Two main types of primitives are currently used in quantum chemical calculations. The first category is given by the Slater Type Orbitals (STO) with the general form:

$$\varphi_{\zeta,n,l,m}(r,\theta,\varphi) = NY_{l,m}(\theta,\varphi)r^{n-1}\exp(-\zeta r) \quad (1.2.2)$$

The second category is based on the Gaussian Type Orbitals (GTO) with the general form:

$$g_{\alpha,n,l,m,f}(r,\theta,\varphi) = NY_{l,m}(\theta,\varphi)r^{2n-2-l}\exp(-\alpha f^2 r^2) \quad (1.2.3)$$

where the α constant determines the spatial extension of the primitive and the f constant is a scaling factor that take into account the more restricted form of the primitives centered on a given atom in a molecule compared to the free atom case.

Currently, the very large majority of calculations on electronic structures of molecules use Gaussian Type Orbitals for expanding molecular orbitals.

The valence orbitals can be represented by one or more basis functions and depending on their number, the basis sets are called valence double, triple, or quadruple-zeta basis sets.

Extended basis sets include polarization functions and diffuse basis functions. Polarization basis functions will describe the influence (distortion, polarization) of the neighboring nuclei on the electron density near a given nucleus. In order to take this effect into account, orbitals that have more flexible shapes in a molecule than the s, p, d, etc., shapes in the free atoms are used. In practice, a set of Gaussian functions one unit higher in angular momentum than what are present in the ground state of the atom are added as polarization functions.

For excited states and anions where the electronic density is more spread out over the molecule, some basis functions which themselves are more spread out are needed (i.e. GTOs with small exponents). These additional functions are called diffuse functions and they are normally added as single GTOs.

For practical applications, the most used basis sets are the so-called Pople style basis sets with the general notation:

k-nlm++G(idf,jpd)

where:

k is the number of GTO primitives used to expand the core orbitals, n is the number of GTO primitives used to expand the inner valence orbitals, l is the number of GTO

primitives used to expand the medium valence orbitals, m is the number of GTO primitives used to expand the outer valence orbitals, + means that 1 set of P (SP) diffuse functions are added on heavy atoms, ++ means that 1 set of P (SP) diffuse functions added to heavy atoms and 1 s diffuse function added to H atom.

idf means that i d sets and 1 f set of polarization functions are added on heavy atoms.

idf,jpd means that i d sets and 1 f set polarization functions added to heavy atoms and j p sets and 1 d set of polarization functions are added on H atoms.

1.3 ONIOM methodology

Quantum chemical calculations on large molecules or molecular complexes is extremely time consuming and it requires huge memory and storage resources. To make such calculations feasible, hybrid methods have been proposed by Honig and Karplus [Hon71] and developed latter by Warshel and Karplus [War72], Warshel and Levit [War76] and Morokuma and his collaborators [Hum96] (for a recent review see ref. [Chu15]). Currently, the method is called ONIOM and the whole system to be investigated is partitioned in two or more layers and different layers are treated at different levels of theory. Usually, the real system is decomposed in two parts, the low layer (the largest part or the environment) and the high layer (the smallest part or the model system) and for the low layer molecular mechanics (MM) methods are used, while for the high layer a quantum chemical method (QM) is employed.

However, for treating the low layer one can also semiempirical or *ab initio* methods. If *ab initio* methods are used for both parts of the system, the methodology is called ONIOM(QM1:QM2). In this case, the extrapolated energy of the investigated real system is obtained as the sum of the model system treated at QM1 level ($E_{QM1,\,model}$) and the sum of the real system treated at QM2 level ($E_{QM2,\,real}$) minus the energy of the model system calculated at QM2 level ($E_{QM2,\,model}$):

$$E_{QM1:QM2} = E_{QM1,model} + E_{QM2,real} - E_{QM2,model} \quad (1.3.1)$$

This methodology found numerous useful applications, for a wide variety of organic structures, macromolecules and molecular complexes.

In this thesis we used the ONIOM(QM:QM) methodology for the calculation of Raman spectrum of a 5 molecules cluster of diphenylhydantoin. Such a model required a prohibitively large computational time if treated at QM level as a whole.

Chapter 2
EXPERIMENTAL AND COMPUTATIONAL DETAILS

2.1 Raman spectrometer

Raman measurements have been performed using the Raman Invia Reflex (Renishaw) spectrometer from the Center of Biomolecular Physics, Ioan Ursu Institute, Babeș-Bolyai University. The spectrometer is equipped with six laser excitation sources, covering the spectral range from NUV to NIR: 325, 442, 532, 633, 785 and 830 nm. Other characteristics of the used equipment can be found at www.phys.ubbcluj.ro/raman.

2.2 General experimental details

The active pharmaceutical ingredients investigated in this thesis were purchased from standard commercial sources and used without further purification. Optical absorbance spectra were recorded at room temperature using a Jasco V-670 UV–Vis–NIR spectrophotometer with a slit width of 2 nm, in a quartz cuvette of 1-cm path length.

FT-IR spectra of powdered samples were recorded at room temperature on a conventional Equinox 55 FT-IR spectrometer equipped with an InGaAs detector and by using KBr (Merck UVASOL) tablet samples, with a resolution of 2 cm^{-1} by co-adding 40 scans. The FT-Raman spectra were recorded in a backscattering geometry with a Bruker FRA 106/S Raman accessory with nitrogen cooled Ge detector. The 1064-nm Nd:YAG laser was used as excitation source and the laser power was set to 350 mW and the spectra were recorded with a resolution of 2 cm^{-1} by co-adding 200 scans.

The dispersive Raman spectra of powdered LEV were recorded at room temperature using a multilaser confocal Renishaw inVia Reflex Raman spectrometer equipped with a RenCam CCD detector. The 325, 532, 633 and 785 nm laser excitation lines were used in this study for measuring LEV' Raman spectra.

The ^{1}H and ^{13}C NMR spectra were recorded at room temperature on a Bruker AVANCE NMR spectrometer (400.13 MHz for ^{1}H and 100.63 MHz for ^{13}C, internal standard TMS, solvent D_2O). The spectra were recorded using a single excitation pulse of 11 μs for ^{1}H and 7.5 μs for ^{13}C. [1H, 1H] COSY NMR spectra have been recorded by using a standard COSY45 d1 - π/2 - d2 - π/4 pulse sequence.

2.3 General computational details

Geometry optimizations and frequency calculations were performed with the Gaussian09 software package [Gau09] by using DFT approaches. Through this study, the hybrid B3LYP exchange-correlation functional [Bec93, Lee88, Vos80, Ste94] was used in conjunction with the Pople's split-valence basis sets 6-31G(d), 6-31G+(2d,2p) and 6-311+G(2d,p) [Heh72, Fri84]. In some cases, in order to capture the dispersion interactions we also used the APFD xc [APFD] functional.

Default criteria were used to define the convergence of both the electronic density and molecular geometries. In all cases, frequency calculations confirmed that all the optimized geometries correspond to minima on the potential energy surface.

Boltzmann weighting factors for conformers were derived at room temperature (T=298 K) by using the relative free energies (ΔG). The latter values were obtained from the frequency calculations including thermal corrections to energies [Duc07, Wil14, Jes15, Hal15].

Absorption spectra were calculated using the time-dependent DFT (TD-DFT) methodology [Cas98]. The UV spectral line-shapes are convoluted with Gaussian functions with full width at half maximum (FWHM) which were derived from experimental spectrum. The nature of the excited states has been analyzed using the Natural Transition Orbitals (NTO) formalism proposed by Martin [Mar03]. This formalism offers compact description of the electronic excitations with the advantage that only one or two occupied/virtual pairs of orbitals are enough for a clear interpretation of the physical nature of the excited states involved in absorption and emission processes [Cla06, Lac12, Vel14, Eti14, Mar15].

The calculation of NMR spectra were performed using the GIAO (Gauge-Including Atomic Orbital) method [Dit74, Wol90], implemented in the Gaussian09 package. In order to express the chemical shifts in terms of the total computed NMR shielding tensors, the scaling and referencing factors were derived from linear regression analysis, according to Willoughby et al. [Wil14].

The solvent effects have been considered by using the implicit Polarizable Continuum Model (PCM) [Tom05], using the integral equation formalism (IEFPCM) variant [Sca10].

Chapter 3
CONFORMATIONAL PREFERENCE AND SPECTROSCOPICAL CHARACTERISTICS OF THE ACTIVE PHARMACEUTICAL INGREDIENT LEVETIRACETAM

3.1 Introduction

LEV is a second-generation nootropic drug used in the treatment of partial-onset seizures in patients with epilepsy [Geo14, Gua02, Kha90, Ull09] and other disorders [Far09]. Its interesting pharmacokinetic properties together with its distinct chemical structure and mechanism of action make LEV unique among the marketed antiepileptic drugs [Ull09, Pit05, Son11, Kli16].

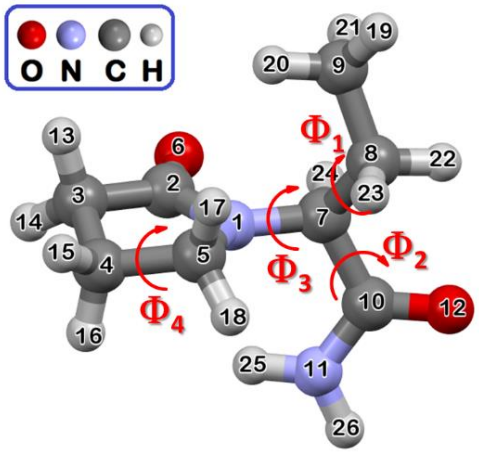

Fig. 3.1 Molecular structure of the most stable conformer of Levetiracetam in water (**5**) at PCM-B3LYP/6-31+G(2d,2p) level of theory.

For a better understanding of the pharmacodynamics of LEV, the characterization of its structure in solid and liquid state is crucial. It was shown that polymorph I of LEV is characterized by an extended network of H-bonding interactions [Son03]. For this reason, a proper model able to include such interactions must be used for a reliable assignment of solid state spectra of LEV. Besides the conformational landscape and the spectroscopical properties of LEV we investigated the possibility to discriminate between different formulations of the brand and generic drugs based on LEV.

3.2 Experimental and computational details

Dispersive Raman spectra of powdered LEV were recorded at room temperature using the Renishaw inVia Reflex Raman spectrometer using four laser excitation lines. In order to check the possibility of discriminating between different formulations of LEV by Raman spectroscopy we used the Keppra™ drug (1000 mg tablet, oral solution – 100 mg/ml and solution for infusion – 100 mg/ml) and the oral solution (100 mg/ml) from Actavis, as well as Actavis, Aurobindo and Terapia tablets. All the samples were obtained from commercial sources on the free market.

The conformational space of LEV in vacuum was explored by using the MMFF94 molecular mechanics force field and DFT quantum chemical calculations.

Absorption spectra of LEV were calculated, both for monomeric and dimeric species, at B3LYP/6-31G+(2d,2p) level of theory. The Natural Transition Orbitals (NTO) [Mar03] was used to describe the electronic transitions of LEV.

Vibrational spectra of LEV recorded on powdered samples were assigned by using the monomer models, as well as a cluster model composed of five molecules, able to capture the most important intermolecular hydrogen bonding interactions.

3.3 Conformational landscape of Levetiracetam

Our first aim for this study was to describe the differences between the known solid state geometries of LEV [Her13, Son03] and its liquid (and gas-) phase structures.

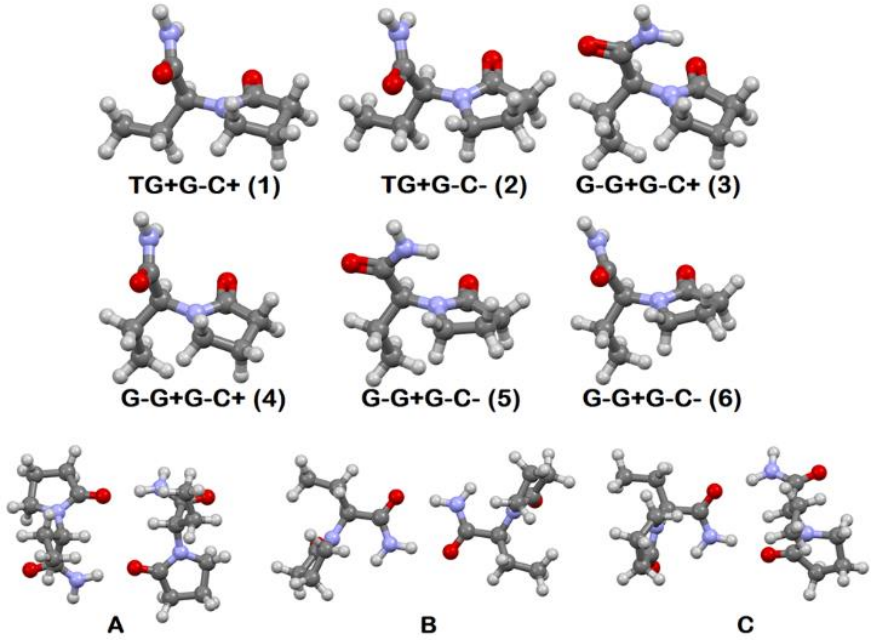

Fig. 3.3 B3LYP/6-31+G(2d,2p) optimized structures of the Levetiracetam monomers and dimers in water: six most stable monomers (**(1)**-**(6)**) and three types of dimmers (A, B, C).
(reproduced from [Luc17])

Twenty-two conformers have been identified and their relative Gibbs energies and Boltzmann statistics were used to predict the room temperature equilibrium populations. The dihedral angles Φ_1 - Φ_4 (see Fig. 3.1) characterizing the 6 most stable conformers shown in Fig. 3.3 are compiled in Table 3.1. The conformers **(1)** - **(6)** are dominant, with a total Boltzmann relative population of 85.8% in gas-phase and 89.5% in water. It is worth

Table 3.1 B3LYP/6-31+G(2d,2p) calculated dihedral angles (degrees) characterizing the levetiracetam conformers in gas-phase, water and ethanol (first, second and third entry, respectively). Experimental data for the known solid state structures of LEV are included for comparison purposes

Conformer	Φ_1	Φ_2	Φ_3	Φ_4	Correspondence to ref. [Li11]
TG+G-C+ (1)	-167.1 -170.9 -170.3	79.2 103.6 100.6	-45.6 -57.3 -56.0	26.6 25.9 26.0	Ib
TG+G-C- (2)	-168.9 -172.3 -172.7	79.1 104.9 105.4	-36.0 -50.3 -50.8	-21.8 -25.5 -26.2	IIb
G-G+G-C+ (3)	-61.3 -59.0 -59.0	77.5 22.3 23.5	-47.7 -55.7 -56.3	27.0 22.2 22.3	not found
G-G+G-C+ (4)	-61.4 -59.5 -59.9	77.5 107.2 91.6	-47.6 -56.0 -55.2	27.0 26.2 25.7	Ia
G-G+G-C- (5)	-65.2 -62.0 -62.0	77.0 18.7 19.4	-40.9 -50.9 -51.3	-20.5 -26.7 -26.9	IIe
G-G+G-C- (6)	-65.2 -63.0 -63.4	77.0 115.0 111.1	-40.8 -49.0 -50.0	-20.6 -25.6 -25.7	IIc
Experimental data					
LEV [Son03]	-54.46	13.65	-58.23	12.92	not available
Etiracetam FI [Her13]	-58.15	33.81	-62.47	-25.13	not available
Etiracetam FII [Her13]	-56.06	39.22	-65.54	-13.95	not available
Etiracetam Hydrate [Her13]	-57.15	20.47	-53.78	-21.54	not available

noting that the most stable conformer in water **(5)** is identical with that resulted in the optimization of the hydrated form of LEV [Her13], while the second most stable conformer **(3)** is identical with that obtained by the optimization of LEV's X-ray structure [Son03]. When used as starting geometries in water, the conformations found in the two polymorphic forms of etiracetam, both converged to conformer **(5)**.

With respect to the work of Li and Si [Li11], the only agreement is observed for the conformer **(1)** that was commonly identified as being the most stable in gas-phase. Instead, for water solvated structures, Li and Si found their **Ia** conformer as being the most stable, while our similar conformer **(4)** is 0.55 kcal mol^{-1} destabilized with respect to the most stable conformer **(5)** found in this work.

The conformational space of LEV in gas-phase is quite distinct from those in water and ethanol solutions. For a particular conformer, the Φ_4 dihedral that defines the chair or

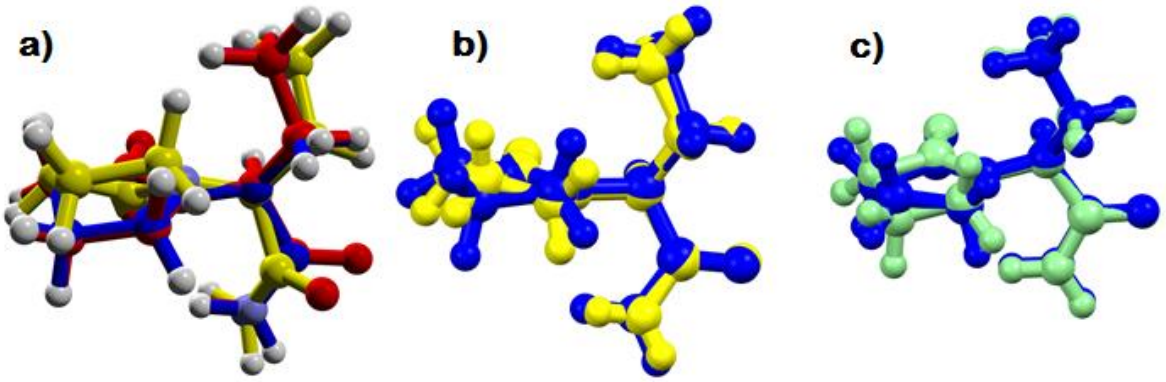

Fig. 3.5 a) B3LYP/6-31+G(2d,2p) optimized molecular structures of the conformer (5) of LEV in gas-phase (yellow), water (blue) and ethanol (red). PCM model was used for implicit solvation in water and ethanol. **b)** Comparison between the geometries of X-ray structure of LEV (yellow) and the optimized conformer (5) in water (blue). **c)** Superimposed structures of the conformers (3) (blue) and (5) (light green) in water. (reproduced from [Luc17])

boat conformation of the oxopyrrolidin ring changes appreciably between the gas and liquid phases only for **(2), (3)**, **(5), (6)** and **(11)** conformers.

Presumably, crystal packing effects overcome intramolecular hydrogen bonding in solid state. This happen because for LEV, both the amino and carbonyl groups prefer the formation of intermolecular HBs with the neighboring molecules in solid state.

It is important to note that the structures of the most stable conformer **(5)** in water and ethanol are almost identical to the X-ray geometry of solid state LEV, both in its conformation and geometrical parameters (see Fig. 3.5 a) and b)) [Son03].

Most probably, this fact explains the similar pharmacokinetic profiles for the liquid and solid formulations of LEV observed by Coupez *et al.* [Cou03]. Moreover, according to data presented in Table 1, the two most stable conformers in water (5) and (3) are also almost identical, the largest difference between them being noted again for conformation of the oxopyrrolidin ring (see Fig.3.5 c) for an easier visual comparison).

Four polymorphic forms have been previously reported for LEV [Par04, Tha09, Xu14]. Based on the single crystal X-ray diffraction data of Song et al. [Son03] and using the ReX software [Bor09] we computed the X-ray powder diffraction pattern which is in excellent agreement with that corresponding to the polymorphic form IV [Tha09], as well as with that reported by Xu et al. [Xu14]. This finding confirms that these polymorphic forms are identical and the form IV is determined by the conformer (3).

Considering the possible clusterization of LEV we tested, by computational means, the possibility of dimerization of S enantiomers (non-hydrated as well as the hydrated homochiral SS dimers). It was demonstrated that A-type dimers are formed as a result of two hydrogen bonds of the same type (H26N11...O6'), i.e., through the amide group from one monomer and the pyrrolidin oxygen atom from the second monomer. B-type dimers are formed through two amide-amide hydrogen bonds (O12...H25'N11'), whereas the C-type dimers are due to two different, amide-amide and amide-pyrrolidin hydrogen bonds (O6...H25'N11' and O12'...H26N11).

Relative free energies and Boltzmann populations of the 11 investigated dimers in water are given in Table 3.6. Interestingly, the most stable non-hydrated homochiral dimer is that of A conformation composed from conformer (1), even though this monomer is not the most stable in water, but in gas-phase. Next stable homochiral dimers, with relative Boltzmann populations greater than 10% are: two C-type dimers composed of monomer (5) and (3), respectively, and one B dimer composed of monomers (5). Also, it is worth mentioning that the non-hydrated homo-chiral dimers are at least 0.36 kmol mol^{-1} less stable than the hetero-chiral dimers. This difference increases to 4.76 kcal mol^{-1} in case of hydrated dimers.

Table 3.6. Relative free energies and Boltzmann populations of the investigated dimers in water at room temperature, calculated at B3LYP/6-31+G(2d,2p) level of theory show in Fig.3.6

	ΔG(kcal·mol^{-1})*	Boltzmann relative population (%)*
SS non-hydrated dimers		
A_m1_SS	0.00	25.38
A_m3_SS	1.43	2.28
A_m5_SS	0.88	5.72
B_m1_SS	0.87	5.88
B_m3_SS	1.07	4.18
B_m5_SS	0.51	10.77
C_m1_SS	0.61	9.03
C_m3_SS	0.41	12.68
C_m5_SS	0.03	24.09
Hydrated dimers		
SS c1	0.07	47.14
SS c2	0.00	52.86

*Values in parentheses correspond to the whole set of SS and RS dimers taken together.

As seen in Table 3.6, the two conformations of the homo-chiral SS dimers are separated by only 0.07 kcal mol^{-1}, with **c2** configuration being the most stable.

Thus, according to computational data, the homo-chiral dimerization is possible in a pure enantiomeric liquid ensemble of monomers but in racemic mixtures the preference for hetero-chiral dimers is obvious.

3.4 UV-Vis spectra of Levetiracetam

A red-shift of the absorbance peak, from 191 nm to 195 nm, is observed by increasing the concentration within the 0.4 M ÷ $1.6 \cdot 10^{-4}$ M range. The simulated UV-Vis spectra were obtained for mixtures of monomers and dimers. The relative Gibbs energies (ΔG) and populations suggest that the predominant contribution to UV-Vis spectra of in water comes from the six most stable monomers **(1)-(6)** that constitute more than 89% of the total population.

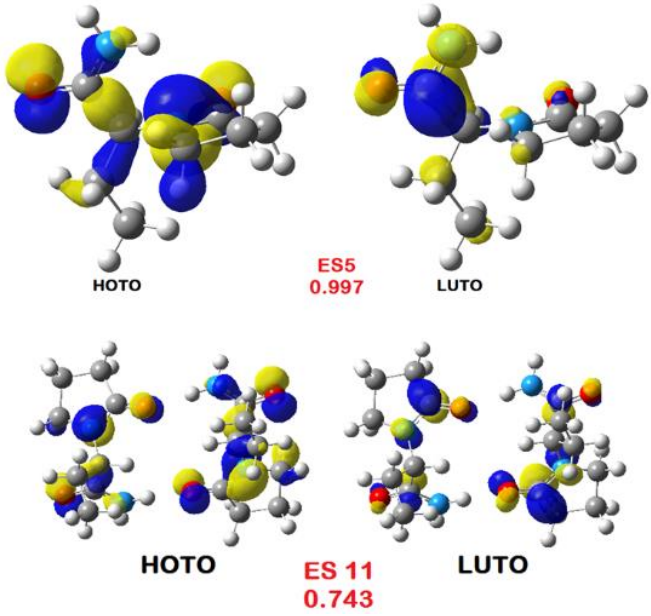

Fig. 3.8 B3LYP/6-31+G(2d,2p) calculated hole (HOTO) and particle (LUTO) natural transition orbitals (isovalue 0.04 a.u.), as well as their coefficients, involved in the electronic transitions with appreciable oscillator strength for the excited state 5 of the Levetiracetam monomer (top) and the excited state 11 of the A_m1 SS dimer (bottom) in water.

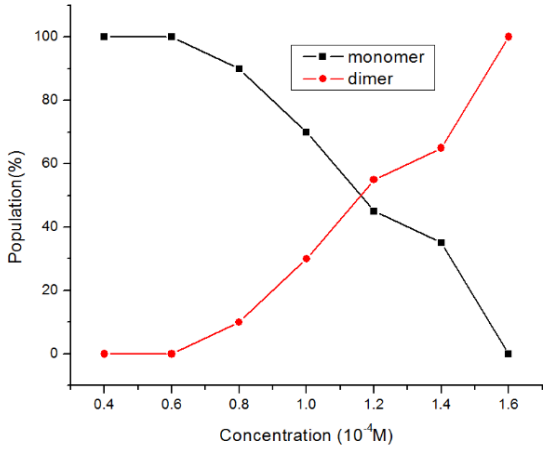

Fig. 3.9 The estimated evolution of the populations of monomers and dimers of Levetiracetam as a function of concentration in water. (reproduced from ref. [Luc17])

According to computational data, for concentrations lower than $0.6 \cdot 10^{-4}$ M, only monomers are supposed to exist in solution. For concentration within the $0.8 \div 1.6 \cdot 10^{-4}$ M, the fraction of monomers decreases at the expense of the increasing fraction of dimers, passing from 89% monomer in

solution at $0.8 \cdot 10^{-4}$ M concentration through intermediate values of 69%, 40%, 35% down to 0% at $1.6 \cdot 10^{-4}$ M. At the maximum concentration of $1.6 \cdot 10^{-4}$ M, the solution is formed only from dimers and the peak wavelength is 195 nm.

Fig. 3.8 illustrates the NTOs for the main electronic transitions of the most stable monomer (5) and dimer (A_m1 SS) of LEV in water. As it can be observed in Fig. 3.8, the most intense transition of the monomer, can be assigned to the intra-molecular charge transfer between the oxopyrrolidin and amide groups. The shapes of NTOs corresponding to the most intense electronic transition for dimers suggest an opposite charge transfer from the butanamide group to the carbonyl unit in the oxopyrrolidin ring, in both monomers.

3.5 NMR analysis of Levetiracetam in water

The experimental and theoretical chemical shifts of LEV (^{1}H and ^{13}C NMR spectra) are summarized in Table 3.9 [Luc14]. The first six most stable monomers in water, constituting 89.5 % of total population were taken into account for chemical shift calculations. Apart from this, we also considered the four most stable non-hydrated homochiral dimers (A_m1, C_m3, B_m5 and C_m1 whose relative Boltzmann population is 72.44 %) as well as the two c1 and c2 SS dimers.

Table 3.9 Experimental and theoretical chemical shifts (in ppm) for Levetiracetam in D_2O. Theoretical data correspond to the six most stable monomers in water, the four most stable – non-hydrated homochiral dimers in water and the two hydrated SS dimers in water.

Nucleus	Experimental data	Monomers in water	Non-hydrated dimers in water	Hydrated dimers in water
C2	178.53	178.81	178.47	178.95
C10	174.27	173.89	174.16	173.28
C7	55.91	56.24	55.81	56.73
C5	44.04	43.46	44.39	44.81
C3	30.40	30.86	30.72	29.58
C8	20.89	21.30	21.73	20.54
C4	17.13	17.70	17.76	17.10
C9	9.43	8.33	7.57	6.97
H26	7.61, s	7.34	8.04	6.79
H25	7.10, s	6.75	6.60	7.40
H24	4.49, 1H, dd	5.40	4.64	5.08
H17, H18	3.49, 2H, t	3.82	3.47	3.91
H13, H14	2.48, 2H, t	2.48	2.38	2.39
H15, H16	2.08, 2H, quin	1.97	2.04	2.06
H23	1.90, 1H, m	2.15	2.11	1.45

H22	1.72, 1H, m	1.40	1.58	2.00
H19-H21	0.86, 3H, t	0.42	0.97	0.36

The largest discrepancies between the experimental and calculated (Boltzmann population-averaged) chemical shifts for monomeric species are noted for C9 and H19-21 nuclei belonging to the ethyl side chain, as well as for the H24 proton. As seen in Table 3.9, the non-hydrated dimers model improves significantly the agreement between experiment and theory for almost all the nuclei. On the other hand, the hydrated dimers give slightly worse theoretical results when compared to either the non-hydrated dimers or to monomers. The averaged unsigned errors are in this case 0.83 and 0.36 ppm for ^{13}C and ^{1}H nuclei, respectively.

The 1D NMR spectrum shows that the peaks corresponding to the H13-14 and H17-18 pairs are triplets due to the vicinal ^{3}J coupling with the H15-16 protons, while the peak of the last pair is a quintet due to the almost equivalent coupling with the four protons of the neighbor methylene units.

In the 2D COSY $^{1}H–^{1}H$ NMR spectrum, the stronger off-diagonal peaks are assigned to the correlation between the geminal proton pairs (H22, H23), followed by proton pairs with ^{3}J couplings: (H13-14, H15-16), (H15-16, H17-18), (H22-H19-21) and (H23-H19-21). Thus, considering the present results we can conclude that the experimental NMR spectrum of LEV in water at the working concentration of $5 \cdot 10^{-2}$ M can be safely assigned based on the dimers model. These NMR data correlate qualitatively with the UV-Vis data which predict the prevalence of dimeric structures at concentration larger than $1.5 \cdot 10^{-4}$ M. Moreover, our results suggest that the direct dimerization of the LEV's monomers is preferable to the formation of the hydrated dimers in which the monomers are interconnected via water molecules.

3.6 Vibrational features of Levetiracetam

3.6.1 Vibrational spectra of the pure Levetiracetam pharmaceutical ingredient

Experimental Raman spectra of LEV are given in Fig. 3.12, while the FT-IR spectrum is shown in Fig. 3.13. The mode assignments were aided by direct comparison between experimental and calculated spectra by considering both the frequency sequence and the intensity pattern and by comparisons with vibrational spectra of similar compounds like piracetam [Kha90, Kse10] butyramide [Lin91] or pyrrolidine [Gog01]. In order to model properly the intermolecular hydrogen bonding interactions

for LEV in solid state, a cluster of five LEV molecules was constructed, where the internal LEV molecule was left to vibrate freely, surrounded by four frozen LEV molecules.

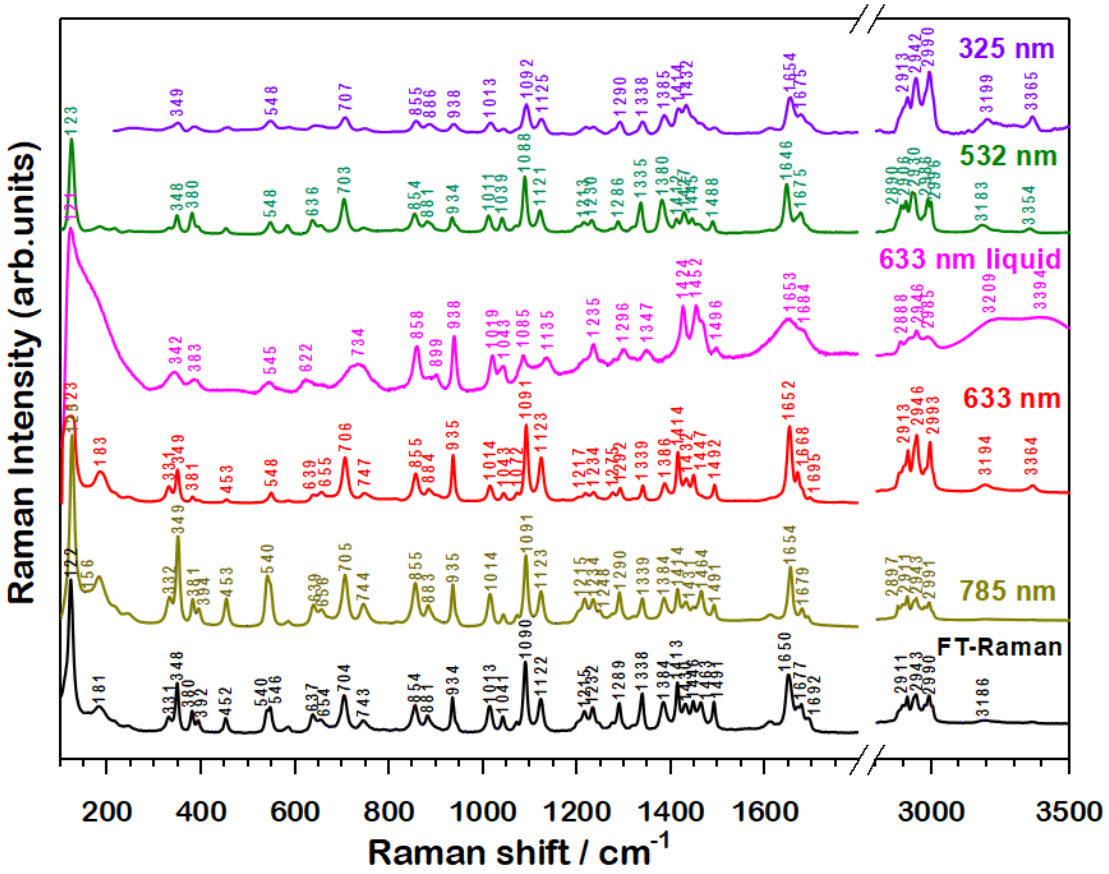

Fig. 3.12. FT- and dispersive Raman spectra of powdered Levetiracetam. Raman spectrum of LEV in aqueous solution (concentration: 1 M) is also included for comparison purposes.

As seen in Fig. 3.12, the experimental FT- and dispersive Raman spectra of LEV are dominated by very strong peaks observed around 1650 cm^{-1} due to amide I vibrations (see Table 3.11), those bands being the most intense in the FT-IR spectrum (see Fig. 3.13). Other characteristic Raman bands are observed around 1414, 1123, 1091, 935, 855, 706, 348 and 123 cm^{-1} in the spectrum excited with the 633 nm laser. Large discrepancies were noted between our both, experimental and computational data and the corresponding data in ref. [Ren14]. Most probably, the experimental discrepancies are due to differences in the purity of the samples, while theoretical mismatch can be assigned to the fact that the above mentioned authors did not use the lowest energy conformer of LEV for vibrational analysis.

Almost all the vibrational bands of LEV have been reassigned in the present study, based on the careful comparison of the IR and Raman spectra and considering the

intensity patterns of the calculated and experimental spectra. Moreover, the comparison of the solid and liquid state spectra of LEV helped unambiguously in the assignment of normal modes to different groups in the molecule, as shown below.

Comparing the aqueous solution spectrum with the solid state Raman spectra in Fig. 3.12, important changes can be noted when going from solid to liquid state of LEV. We concluded the involvement of the amide group in intermolecular interactions with water molecules in liquid state. On the other hand, there are clear evidences suggesting that the oxopyrrolidin and ethyl groups are not affected by intermolecular interactions. Experimental observations are nicely reproduced by cluster model this behavior can be explained by the fact that such a model takes into account the intermolecular interactions which are expected to affect significantly the vibrations of the involved functional groups. For the entire Raman spectrum, the cluster model provides a root mean square deviation of residuals significantly better than the monomer, i.e. 23.6 cm^{-1} vs 33.2 cm^{-1}. If the two (generally problematic) symmetric and asymmetric stretchings vibrations of NH_2 group are excluded, the RMSD values drop dramatically to 10.6 cm^{-1} and 10.3 cm^{-1} for monomer and cluster, respectively.

We conclude this section by emphasizing the necessity of suitable computational models when trying to simulate the vibrational spectra in different states. The model must be adapted so that to catch the most important interactions in reasonable manner.

The reliability of the LEV's normal mode assignments is supported not only by the match between the experimental and computed wavenumbers but also by the reasonable good agreement between the observed and calculated intensities.

3.6.2 Raman spectra of Levetiracetam's Drugs

In order to check the possibility of discriminating between different formulations of LEV by Raman spectroscopy we used the Keppra™ drug, 1000 mg tablet, Keppra™ oral solution – 100 mg/ml and solution for infusion – 100 mg/ml and the oral solution (100 mg/ml) from Actavis, as well as Actavis 1000 mg tablet. Raman spectra of the liquid phase drugs are shown in Fig. 3.15.

First we note a large degree of similarity between the aqueous solution of LEV and the injectable (infusion) formulation of Keppra™. While again very similar, the spectra of the two oral formulations (Keppra™ and Actavis) show, however, a clear difference consisting in the doublet observed at 1768/1760 cm^{-1} only for the Keppra™ drug.

Such a doublet is not observed either in the powdered sample or in the liquid LEV compound, but it can be seen as a very weak signal for the Keppra's (oral and infusion) solutions. Our calculations of the Raman spectra of the excipients used in the two

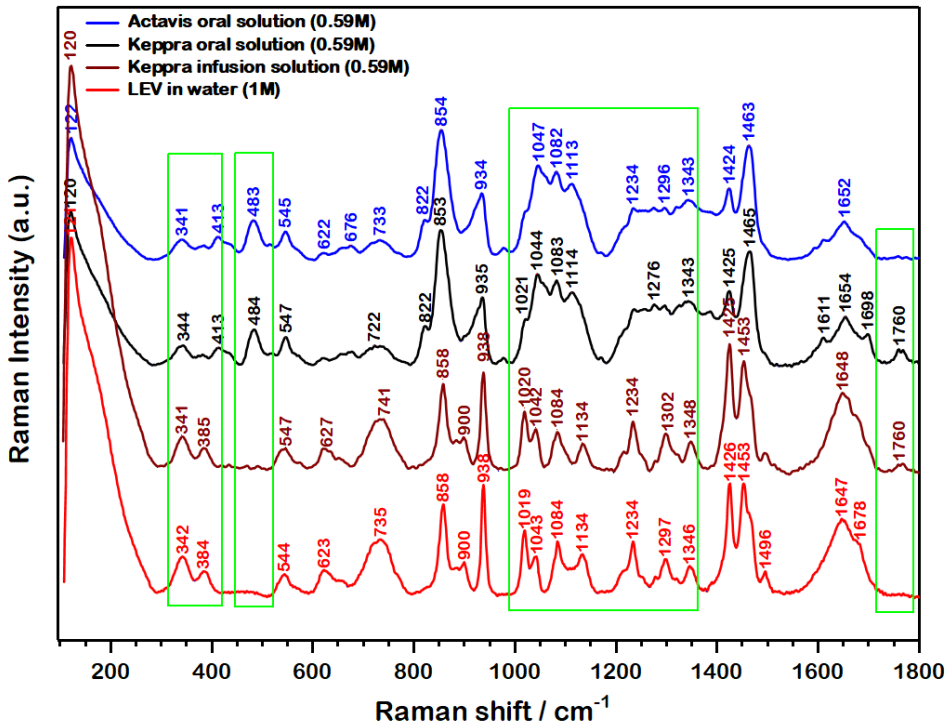

Fig. 3.15 Raman spectra of the investigated LEV drugs (excitation laser line: 633 nm). From bottom to top: LEV in water (1M); Keppra™ solution for infusion (0.59M); Keppra™ oral solution (0.59M); Actavis oral solution (0.59M)

formulations suggest that these bands can be assigned to the citric acid monohydrate for which a doublet of strong bands was calculated at 1765 and 1740 cm^{-1}, corresponding to the in-phase and out-of-phase C=O stretchings. Moreover, the peaks observed at 1611 and 1698 cm^{-1} in the Raman spectrum of oral solutions, more distinct for the Keppra™ drug are assigned to the methyl-paraben excipient for which two very strong Raman bands are predicted: ν(C=O) at 1680 cm^{-1} and ν(C=C) at 1588 cm^{-1}, in very good agreement with experimental data.

Comparing the oral formulations of Keppra™ and Actavis with the injectable Keppra™ formulation we note many differences, most probably due to the excipients used for the two formulations. Considering the normal mode assignments, all the changes point to the fact that oxopyrrolidin group is affected differently in the two investigated formulations of LEV.

The Raman spectrum of the Keppra™ solid formulation (tablet) was collected focusing the laser on the tablet's surface, as well as by measuring the inner powder..

The Raman bands observed on the tablet's coating are characteristics for TiO_2 anatase phase (395, 514 and 638 cm^{-1}) [Ohs80, Bal82] and polyethylene glycol 3350 (1480, 1442, 1278, 1231, 1141, 1125, 859 and 843 cm^{-1}) [Vei09, Ict15]. On the other hand, the two spectra given by the interior powder of the tablet are very similar to each other and to the pure LEV chemical compound. Comparing these spectra with that of the LEV compound leads to the conclusion that no interaction take place between the API and the excipients used for the solid formulation.

Raman spectra recorded inside the tablet formulations from different manufacturers show no significant difference in case of the same quantity of API. On the other hand, the Raman spectrum recorded for the Actavis 500 mg tablet shows an intense fluorescence signal. Also, the Aurobindo tablet shows a weak Raman peak at 476 cm^{-1}, which is not observed in the spectrum of the pure LEV compound or in the spectra of Keppra™ and Actavis tablets.

To the best of our knowledge, the low frequency Raman spectrum of LEV has never been reported in the literature so far. According to our experimental data five distinct bands (32, 64, 75 and 97 cm^{-1}) can be observed in the low-frequency region of the Raman spectrum of powdered LEV compound. Such bands are commonly assigned [Kin11, Hed13] to the intermolecular and/or lattice vibrations of the investigated compounds and they are extremely useful for distinguishing different polymorphic forms of the drugs [Dat04]. Even though the assignment of these bands is beyond the scope of this work, the presented low-frequency Raman spectrum might be useful as a reference of the LEV API in solid state formulations as a unique signature for discriminating between eventually different polymorphs, or for controlling the crystallinity of LEV-based pharmaceuticals and the transformation of the drug during the manufacturing.

3.7 Conclusions

Twenty two conformers have been identified for the monomer, the most stable 6 in water having a total Boltzmann population of 89.5%.

The most stable conformer in water is identical to that resulted in the optimization of the hydrated form of LEV, while the second most stable conformer is

identical with that obtained by the optimization of LEV's X-ray structure. The geometries of the two conformers are very similar and very close to the X-ray structure and most probably this finding explains the similar pharmacokinetic profiles for the liquid and solid formulations of LEV.

Two different conformations with a difference in Gibbs free energy of 0.07 kcal*mol^{-1} were found for the hydrated dimers and the theoretical results, as well as NMR data suggest that the direct dimerization of the LEV's monomers is preferable to the formation of the hydrated dimers.

The most intense electronic excitations are dominantly driven by intramolecular charge-transfer type transitions, from oxopyrrolidin to amide unit for monomer and from the butanamide groups to the carbonyl units in the oxopyrrolidin rings for dimer.

The non-hydrated dimers model improves significantly the agreement between experimental and computed chemical shifts of LEV.

Compared to the previous vibrational investigation of LEV, most of the Raman bands have been re-assigned in this study, based on DFT calculations performed on monomer and cluster models.

According to calculations, the most affected bands by the solid-liquid-phase transition were those associated with vibrations involving the amide group, confirming the involvement of this group in intermolecular interactions in liquid state, too.

Using Raman spectroscopy we were also able to distinguish between different formulations of the same manufacturer or between the same solid formulations of several manufacturers. Our data suggest that the oxopyrrolidin group is affected differently in case of the two liquid formulations of the Keppra™ drug.

Tracking both the solid and liquid phases of LEV, the present results could help for a better understanding of the structural transformation of the molecule between the two states and of the solvent-mediated polymorphic transformation of etiracetam. Moreover, we demonstrated that the conformer obtained from the hydrate form is the most stable in water and this result could be useful for searching a hydrate form of the S enantiopure compound.

Bringing detailed spectroscopic features of the brand drug in different formulations, the results presented in this work could also be useful for the Raman analysis of the counterfeit LEV-based drugs.

Chapter 4
MOLECULAR STRUCTURE AND VIBRATIONAL FEATURES OF DIPHENYLHYDANTOIN

4.1 Introduction

Phenytoin (DPH) is the oldest non-sedative antiepileptic drug [Cam71, Huq07] indicated for the treatment of epilepsy [Cha78], which acts by decreasing the excitatory neurotransmission and enhancing γ-aminobutyric acid - mediated inhibition. However, despite being extensively used as an active pharmaceutical ingredient for antiepileptic drugs its "biological face" [Tie08] still remains incompletely elucidated.

Like for all the anticonvulsant drugs, the distance between the center of the phenyl ring and carbonyl oxygen is considered important, because both groups are thought to bind to the receptor site on the sodium channel [Mar06]. The modification of hydrogen bonding groups can decrease or even stop the anticonvulsant activity [Pou84, Cor85]. The great interest in the properties of DPH prompted us to study the dimerization process of DPH through hydrogen bonding interactions. Thus, a thorough conformational analysis of the dimeric species following the Boltzmann's distribution law is presented in this work. Moreover, combining the experimental UV-Vis and NMR techniques with quantum chemical calculations we addressed the effect of such hydrogen bonding interactions on the electronic transitions as well as on the NMR chemical shifts of DPH. In the last part of this chapter we addressed the vibrational features of DPH.

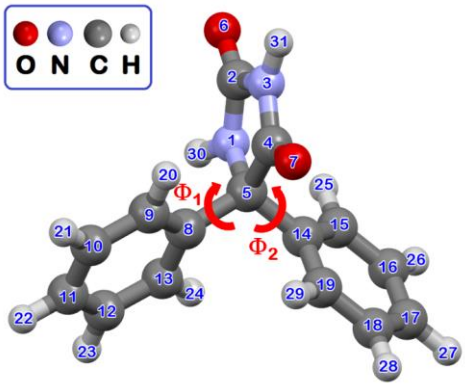

Fig. 4.1 B3LYP/6-31+G(2d,2p) optimized molecular structure of the most stable conformer of phenytoin in gas-phase

4.2 Experimental and computational details

Optical absorbance spectra of DPH in ethanol were recorded at room temperature using a Jasco V-670 UV–Vis–NIR spectrophotometer with a slit width of 2 nm. The ^{1}H and ^{13}C NMR spectra were recorded at room temperature on a Bruker AVANCE NMR spectrometer (400.13 MHz for ^{1}H and 100.63 MHz for ^{13}C, internal standard TMS). The samples were prepared by the dissolution of DPH in DMSO (signal

for ^{1}H at 2.51 ppm and at 39.45 ppm and for ^{13}C). The Raman and low frequency Raman spectra of DPH powder were recorded at room temperature using a Renishaw inVia Reflex Raman Microscope equipped with a RenCam CCD detector. The 532 and 785 nm laser excitation lines were used in this study.

The optimization of DPH geometry and single point calculations were performed with the Gaussian 09, revision C.01 software package [Gau09] by using DFT approaches. The hybrid B3LYP [Bec93, Lee88, Vos80, Ste94] and APFD [APFD] exchange-correlation functionals were used in conjunction with Pople's split-valence basis sets [Heh72, Fri84]

Absorption spectra of DPH were calculated at TD-B3LYP/6-31+G(2d, 2p) level of theory. The calculation of NMR chemical shifts for DPH was performed using the GIAO (Gauge-Including Atomic Orbital) method [Dit74, Wol90], with the B3LYP exchange-correlation functional, in conjunction with 6-31+G(2d,2p) basis set.

For modeling the vibrational spectra of DPH we used the cluster model composed of 5 molecules. For this model we employed the ONIOM QM:QM approach, treating the relaxed molecule and the neighboring molecules at B3LYP/6-311+G(2d,p) and B3LYP/3-21G level of theory, respectively. Moreover, for the monomer model we tested the performance of the anharmonic approximation in reproducing the Raman spectrum.

4.3 Hydrogen bonding interactions of diphenylhydantoin

Two minimum energy structures are possible for the DPH monomer, i.e., the structure shown in Fig.4.1 (denoted as A conformer) and its mirror image (B conformer). Even though these two minima are equivalent from energetic and spectroscopic point of view, both of them must be considered when forming the possible dimers of DPH [Luc15]. Thus, for conformer A, the left (C8-C9) ring is almost coplanar with the C4-C5 bond of the hydantoin unit, while the second phenyl ring (C14-C15) is approximately coplanar with the C5-N1 bond. Due to the presence of the two NH groups as hydrogen bond donors and two oxygens as hydrogen bond acceptors, different hydrogen bonded dimers can be formed. We were interested only in these type of dimers because they are significantly more stable than other types of dimers, formed for instance by dispersion interactions. Only the double hydrogen bonded dimers were considered here.

A total number of 12 double hydrogen bonded unique dimers can be formed (see Fig. 4.2), of which 6 are of AA type and 6 of AB type. The BB and BA type dimers were not considered because they are mirror images of the AA and AB types, respectively.

Selected structural parameters of some of the 12 unique dimers of DPH are reported in Table 4.1. The geometries of the dimers were fully optimized without imposing any constraints and all of them correspond to minima on the potential energy surface.

We shall first briefly discuss the structural characteristics of the monomer for which geometrical parameters have been reported by Camerman *et al.* [Cam71] and discussed also by Tamir *et al*. [Tam80].

The angles between the planes defined by the phenyl groups and the hydantoin unit are presented in Table 4.2. The best agreement between the experimental and calculated data is again noted for the gas-phase molecule, particularly for the (Ph2,Hyd) dihedral angle. In liquid phase, the angle between the Ph1 and Hyd planes is only slightly changed with respect to gas-phase. On the other hand, the dihedral angle (Ph1,Ph2) decreases in solution, simultaneously with a slight increase of the (Ph2,Hyd) angle. As seen in Table 4.2, the distance between the centroids of the phenyl rings and the carbonyl oxygen atoms is not much affected by the transition between the gas-phase and liquid phase. We also note that there is no qualitative difference between the geometrical parameters that characterize the relative orientation of the phenyl rings to the hydantoin unit for the dimeric structures in gas-phase and ethanol. The same geometry is predicted for the same kind of dimers in the two solvents, which is slightly different from that predicted for the gas-phase.

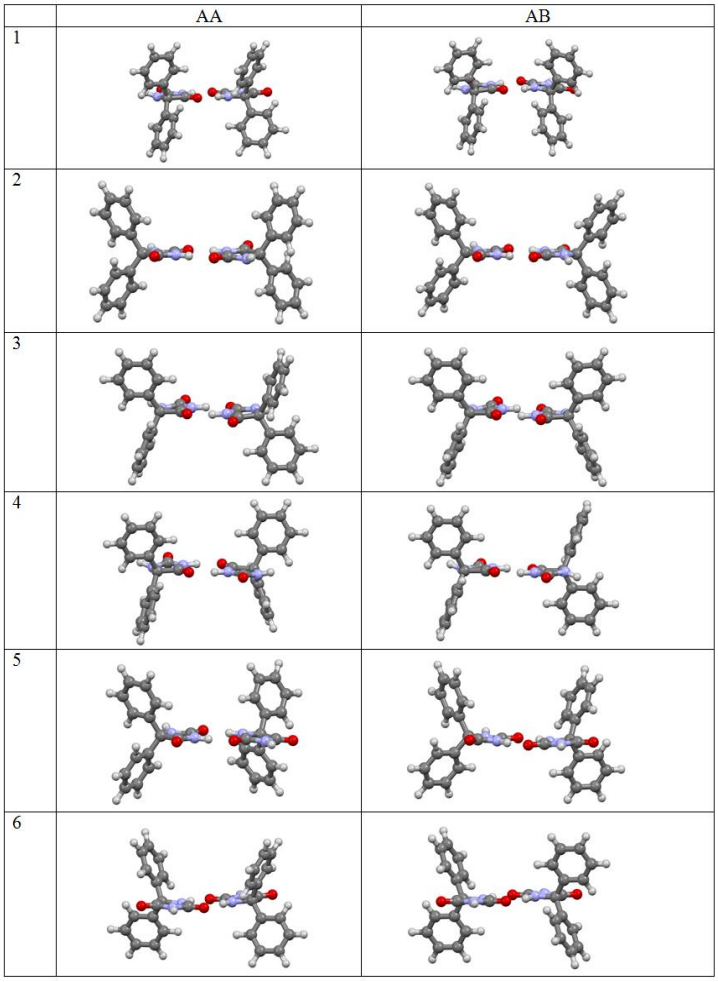

Fig. 4.2 B3LYP/6-31+G(2d,2p) optimized structures for the dimers of DPH in gas-phase.

Table 4.2. Calculated angles (degrees) between planes and distances (Å) between the ring centroids and oxygen atoms for DPH monomer in gas-phase, ethanol and DMSO

Parameter[a)]	gas-phase	ethanol	DMSO	X-ray data [Cam71]
∠(Ph1,Ph2)	81.59	76.03	77.57	89.56
∠ (Ph1,Hyd)	73.32	73.87	73.73	65.67
∠ (Ph2,Hyd)	66.98	70.86	69.87	65.95
d(X1O7)	4.263	4.250	4.253	4.226
d(X2O7)	4.012	4.002	4.003	3.968
d(X1O6)	5.473	5.531	5.528	5.513
d(X2O6)	5.779	5.711	5.715	5.677

[a)] Ph1, Ph2 and Hyd are the planes defined by C8-C13 phenyl ring, C14-C19 phenyl ring and hydantoin ring, respectively; X1 and X2 are the centroids of the two phenyl rings.

Table 4.3 Relative energies (kcal mol^{-1}, ZPE corrected) and Boltzmann populations (%) of the twelve DPH dimers in gas-phase (B3LYP/6-31+G(2d,2p) level of theory) and in ethanol and DMSO (PCM-B3LYP/6-31+G(2d,2p) level of theory), at room temperature

	Gas		**Ethanol**		**DMSO**	
Dimer	**ΔE_{ZPE}**	**Population**	**ΔE_{ZPE}**	**Population**	**ΔE_{ZPE}**	**Population**
1AA	1.22	3.62	0.98	5.75	1.04	5.54
2AA	0.00	14.26	0.02	14.46	0.06	14.19
3AA	1.09	4.50	0.46	13.85	0.46	14.41
4AA	2.07	0.44	1.28	1.73	1.27	1.83
5AA	0.24	19.13	0.53	12.28	0.58	11.81
6AA	0.36	7.77	1.28	1.74	1.36	1.58
1AB	1.47	2.39	1.02	5.36	1.03	5.50
2AB	0.01	14.02	0.00	15.07	0.00	15.66
3AB	1.20	3.79	0.47	13.63	0.48	13.93
4AB	2.11	0.40	1.23	1.90	1.21	2.03
5AB	0.22	19.72	0.54	12.17	0.59	11.63
6AB	0.21	9.97	1.18	2.06	1.26	1.88

It is reasonable to assume that the strength of the HB interactions will play a major role in the stability of the dimers. This is indeed true for the solvated dimers in which case the dimeric structures with the shortest (averaged) HB distance (2AB dimer) are the most stable, the situation being mirrored for the gas-phase structures. For the latter ones, the most stable, nearly isoenergetic dimers 2AA and 2AB have an averaged HB distance of 2.837 Å, significantly shorter than the immediately higher in energy dimers 6AB and 5AB.

The intermolecular hydrogen bonding in the most stable dimer 2AA lead to the increase of the N-H and C=O bond lengths by about 0.021 and 0.014 Å, respectively,

with respect to the monomer. The differences appear because DPH molecule is involved in two hydrogen bonds in all the investigated dimers but in solid state each monomer is connected to four neighbor molecules, making two pairs of equivalent hydrogen bonds of 2.784 and 2.884 Å.

As shown in Table 4.3, our calculations predict a dramatic change in the pattern of relative energies of some dimers when going from gas-phase to liquid-phase. However, the two 2AA and 2AB dimers are the most stable both, in gas-phase and liquid phase. Particularly, the 2AB and 2AA dimers contribute together almost 30 % of the total population in solution. In ethanol and DMSO solvents, the dimers 2AB, 2AA, 3AA, 3AB, 5AA and 5AB are within a 0.59 kcal·mol^{-1}, which is less the room temperature energy. Even though significantly higher in energy, due to the symmetry degeneracy, the dimers 1AA and 1AB have appreciable relative populations, higher than 5%.

4.4 Electronic transitions of diphenylhydantoin

The UV-Vis spectra of DPH in ethanol (see Fig. 4.4) were recorded at five concentrations, ranging from 10^{-5} M to 10^{-4} M. A slight red-shift from 204 nm to 211 nm was observed for λ_{max} by increasing the concentration. According to theoretical results,

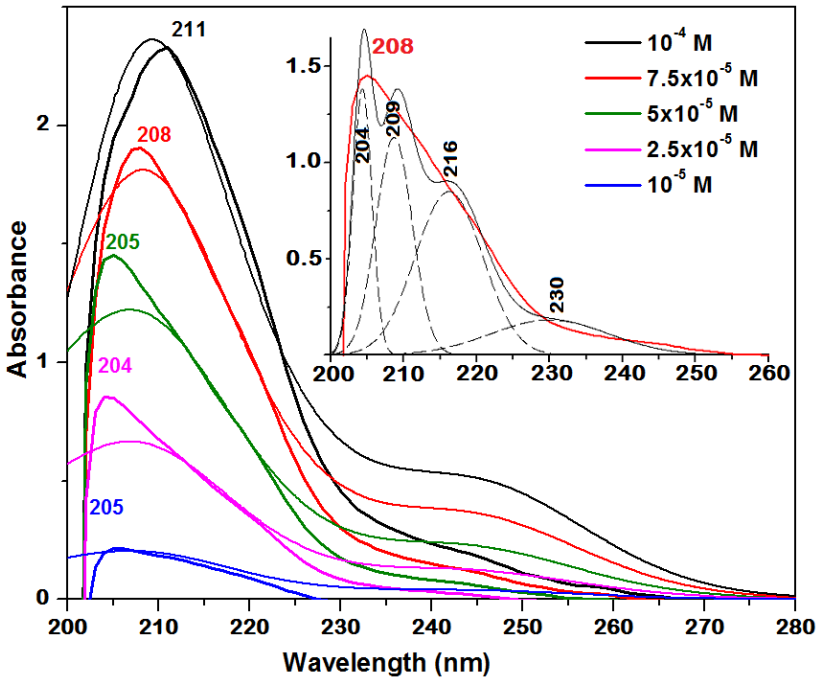

Fig. 4.4 Experimental (solid line) and simulated (dashed line) UV-Vis spectra of DPH in ethanol at five concentrations. Simulated spectra have been calculated for DPH monomer and the eight most stable dimers in ethanol, whose cumulated Boltzmann population is 92.6 % (see Tables 4.4 and 4.5). In the inset is illustrated the deconvoluted experimental curve recorded at 7.5·10^{-5} M.

the most intense electronic transitions of the DPH monomer are predicted in UV region, in very good agreement with the experimental data. The main contribution to S0 → S1 transition is the HOMO-LUMO excitation. We assigned this transition to the intra-molecular charge transfer between the phenyl rings and hydantoin group. The inset in the Fig. 4.4 shows the deconvolution of the experimental UV spectrum at $7.5 \cdot 10^{-5}$ M concentration, with peaks at 204 nm, 209 nm, 216 nm and 230 nm. The first three deconvoluted peaks can be put in correspondence with the first three simulated absorbance bands. Only the last deconvoluted peak at 230 nm is shifted appreciably to lower wavelengths compared to the simulated absorbance band peak at 247 nm.

Based on present calculations we assume that for concentrations lower than $5 \cdot 10^{-5}$ M the dominant contributions to the absorption spectrum is mostly due to the monomers, and the experimental peak is given by the absorption band calculated for monomers at 201-208 nm. A clear asymmetry of the absorption curves is observed for all concentrations. We find that they hide a shoulder near 230 nm that can be recovered by deconvolution (see the inset in Fig.4.4).

The red-shift of λ_{max} (from 205 nm to 211 nm), observed as a result of increasing the concentration, can be explained by the increase in dimer population, which is assumed to occur when the concentration increases from $5 \cdot 10^{-5}$ to 10^{-4}M. According to the calculated relative free energies, the DPH dimers 2AB and 2AA are the most stable and most abundant in ethanol. Expectedly, the UV spectra of the other seven dimers have similar electronic absorptions with those of 2AB dimer, in the same wavelength regions. Based on monomer and dimer model calculations we consider that the experimental peak at λ=205 nm in Fig. 4.4 indicates the absorption by 100% population of monomers; Also, the monomer population is dominant for concentrations lower than $5 \cdot 10^{-5}$ M. The intermediate UV curve with the peak at λ=208 nm is the result of absorption of a mixed population of 50% monomers and 50% dimers. The experimental peak at λ=211 nm is due to a 100% population of dimers.

4.5 NMR analysis of diphenylhydantoin

The experimental and calculated (population averaged) chemical shifts, both for monomer and the twelve investigated dimers of DPH in DMSO, are listed in Table 4.6.

As it can be seen, the main differences between experimental values and those calculated for monomer are noted for the C5 nucleus as well as for the H30 and H31 protons. The hydrogen-bonding interactions can affect the shielding of H30 and H31

Table 4.6 Experimental and theoretical chemical shifts (in ppm) for DPH in DMSO

Atoms	Experimental data[a)]	Theoretical data[b)]	
		Monomer	Dimer
C4	174.81	174.73	174.40
C2	156.00	153.99	156.32
C8,C14	139.90	138.87	139.71
C10,C12,C16,C18	128.45	126.89	126.46
C11,C17	127.98	126.70	126.48
C9,C13,C15,C19	126.57	126.14	126.11
C5	70.22	77.70	76.96
H31	11.18	8.40	11.50
H30	9.39	6.67	5.64
H22,H27	7.35	7.99	7.75
H20,H21, H23-H26, H28,H29	7.41	7.84	7.70
MAE	-	1.86	1.49

[a)] The NMR ^{1}H and ^{13}C data of DPH in DMSO with respect to the TMS reference values.

[b)] The chemical shifts calculated at B3LYP/6-31+G(2d,2p) level of theory.; dimer data were derived as a weighted average of the chemical shifts calculated for the eight most stable dimers of DPH in DMSO whose cumulated Boltzmann population is 92.7 %.

protons. This is indeed the case, and dimer calculations show that these intermolecular interactions modify the charge density of the hydantoin unit, having as a result a significant change of the chemical shift of C2 and H31 nuclei and to a smaller extent for the H30 nucleus. The value of chemical shift for the C5 nucleus in dimer improves only slightly compared to the monomer case. The reason must be that the C5 nucleus is shielded by the phenyl rings more strongly than predicted by the PCM continuum solvation model. The 5AB and 1AB dimers provide an improved agreement between the experimental and calculated chemical shift for H30 proton, at the expense of a worse agreement for the H31 proton. Nevertheless, the corresponding calculated values for the individual dimers, as well as the weighted average are unacceptably away from the experimental counterparts. This discrepancy can be attributed to the non-inclusion of the specific solute-solvent interactions in the computational model.

4.6 Vibrational features of diphenylhydantoin

For a reliable assignment of the Raman spectrum of DPH, in this study we based on the comparison with the Raman spectrum of 2,4-imidazolidinedione [Biorad], as well as on the DFT calculated Raman spectra of a cluster composed of 5 DPH molecules and on the calculated anharmonic spectrum of the DPH monomer.

In Fig. 4.6 is given the experimental Raman spectrum of DPH. Fig. 4.8 illustrates the calculated Raman spectrum of DPH using two models with different computational

methodologies. The upper curve represents the calculated spectrum based on the QM:QM methodology where for the low layer comprising the 4 neighboring molecules we used the B3LYP/3-21G level of theory, while for the high level comprising only one molecule which was fully optimized we used the B3LYP/6-311+G(2d,p).

The second computational methodology uses the monomer model solvated in water and the calculations were performed based on the anharmonic approximation [Bar14, Cor16], rooted into the second-order vibrational perturbation theory (VPT2) [Pic15], at APFD/6-311+G(2d,p) level of theory.

As seen in Fig. 4.8, the experimental spectrum is much better reproduced by the cluster model treated within the ONIOM approach in the whole spectral range. We particularly note the excellent agreement for the Raman bands associated with the carbonyl stretches, but also the spectral features observed in the 1072-1234 cm^{-1} and 602-784 cm^{-1} spectral ranges. It is worth mentioning that, besides providing much better agreement with the experimental data, the quantum chemical calculations on cluster model take the advantage of being two orders of magnitude much faster (24 hours and 23 minutes, compared to 3182 hours and 43 minutes for the anharmonic calculations).

The mode assignments were aided by direct comparison between experimental and calculated spectra by considering both the frequency sequence and the intensity

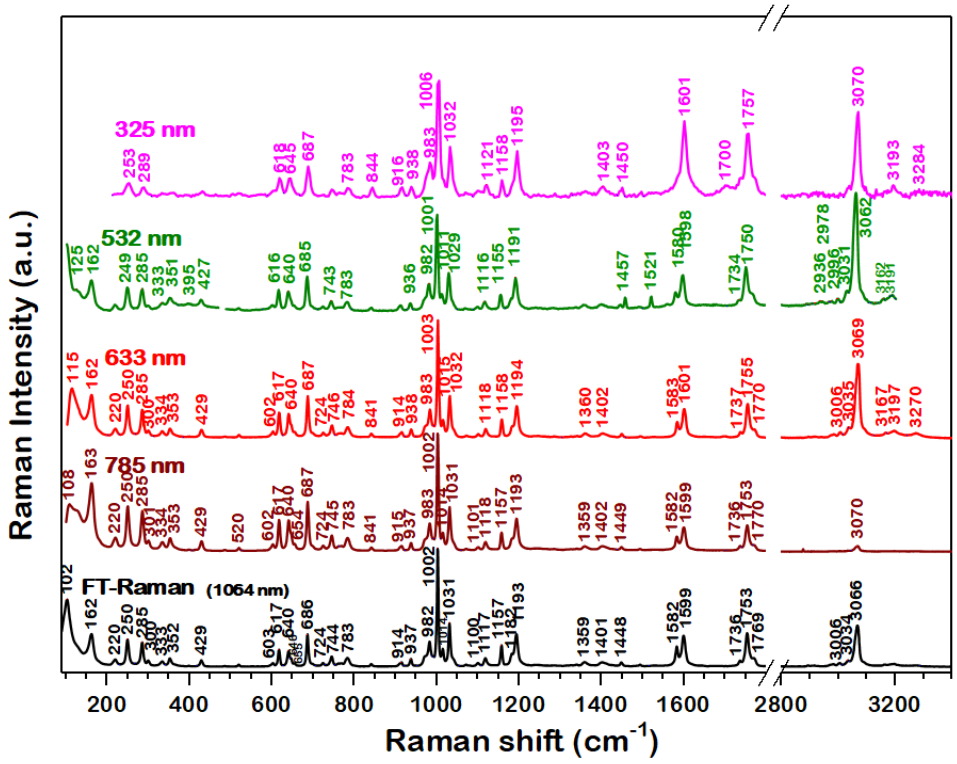

Fig. 4.6 Experimental Raman spectra of powdered DPH at room temperature

pattern and by comparisons with vibrational spectra of similar components like hydantoin [Kim03, Ild12, Biorad] and phenyl radical [Lap01].

We shall first note that the IR bands observed for DPH at 1774 and 1717 cm^{-1} correspond to the most intense experimental IR bands at 1779 and 1717 cm^{-1} for hydantoin. Other IR bands of hydantoin (3265, 1296, 641, and 440 cm^{-1} [Biorad]) observed in the spectrum of DPH are those located at 3272, 1285, 641 and 453 cm^{-1}.
There are also Raman bands characteristic for hydantoin (2977, 1735, 1698, 1071, 1000, 908, 642 and 414 cm^{-1} [Biorad]) that can be seen in the spectrum of DPH very close to their position but with significant lower intensity (2976, 1737, 1698, 1072, 1003, 914, 640 and 429 cm^{-1}). On the other hand, two strong Raman bands in the hydantoin's spectrum at 1422 and 580 cm^{-1} are not observed in the DPH's spectrum.

As seen in Fig. 4.6, at least three peaks can be identified in the Raman and IR spectrum of DPH in the spectral range characteristic for carbonyl group stretchings.
Due to its NH and C=O groups, DPH is available for hydrogen bonding, both in solid state and liquid state. We assigned the bands around 1750 cm^{-1} to free and hydrogen bonded carbonyl groups symmetric and asymmetric stretchings.

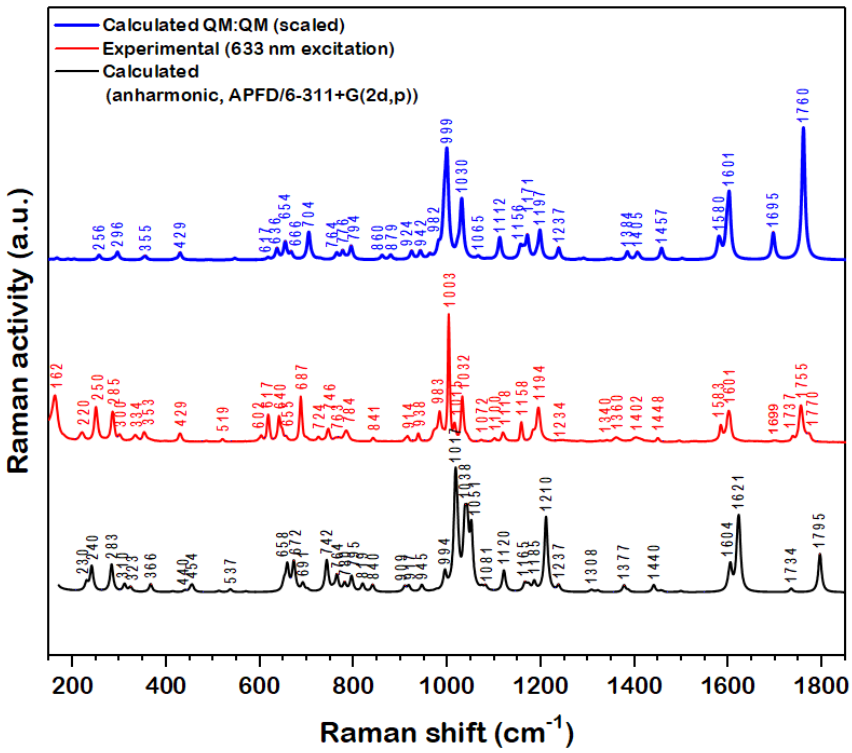

Fig. 4.8 top: QM:QM calculated Raman spectrum of DPH; middle: Experimental Raman spectrum of powdered DPH at room temperature (633 nm laser line); bottom: APDF/6-311+G(2d,p calculated anharmonic Raman spectrum of DPH in gas-phase

Other characteristic Raman bands of DPH are observed at 1601, and 1583 cm^{-1} (633 nm excited spectrum), both of them corresponding to the CC stretchings in the Phenyl groups. The band at 1194 cm^{-1} is due to the stretching between the hydantoin and phenyl groups. No Raman band is observed for hydantoin in this region.

The band at 1003 cm^{-1} (most intense in the Raman spectrum of DPH) is due to a mode involving CCC bendings in phenyl groups as well as CNC bendings in the hydantoing group. The Raman spectrum of pure hydantoin shows a weak band at 1000 cm^{-1}.

It is worth mentioning the presence of a strong band at 1422 cm^{-1} in the Raman spectrum of hydantoin, corresponding to $\beta(CH_2)$ vibrations. Another hydantoin band that vanishes in the Raman spectrum of DPH is seen at 580 cm^{-1} (the out-of-plane deformation of hydantoin coupled to CH_2 rocking vibration). This deformation is hampered in DPH due to the connection to phenyl groups and that explains the extinction of the corresponding band. We emphasize here that reliable assignments of the vibrational bands of complex structures like active pharmaceutical ingredients can only be obtained by analyzing also the spectra of the constituting groups, if available.

We would like to mention also that even though the Raman spectra recorded by using different excitation lasers are very similar in terms of peaks' positions and the relative intensities of nearby peaks, a significant change is observed in the bands' intensities when going from the 325 nm to 785 nm excitation laser lines. Thus, the 785 nm laser gives rise to more intense Raman bands within the 100-800 cm^{-1} spectral region, while in the 800-1800 cm^{-1} the most intense Raman bands are obtained with the 325 nm excitation laser. A significant increase is observed particularly for the Raman bands at 1601, 1757 and 1195 cm^{-1}.

Similar changes were observed previously by Thorley et al. [Tho06]. As in our case, the mentioned work shows that the UV laser gives rise to more intense Raman bands at higher wavenumbers. Nergui et al. [Ner16] have proposed for adenine that such wavelength dependence of the Raman peak intensities could be explained by considering the pre-resonant conditions, even though the wavelength of the excitation lasers are far from resonance. Most probably, the same assumption is valid for the characteristic increase of Raman activities for the higher wavenumber Raman bands of DPH. Another explanation could be the polarizability dependence of DPH on the excitation laser wavelength. Further investigations are needed in order to clarify this behavior.

4.7 Conclusions

The geometrical structures of the monomer and twelve unique dimers of 5,5-diphenylhydantoin have been investigated at B3LYP/6-31+G(2d,2p) level of theory. Calculated relative ZPE-corrected energies for the DPH dimers show that the same two dimers (2AA and 2AB) are most stable in gas-phase and in solution, but an important change in relative stabilities is noted for the remaining set of 10 dimers. For the DPH monomer, the dihedral corresponding to the relative orientation of the two phenyl rings in solution decreases appreciable with respect to the solid state structure, simultaneously with a similar increase in the dihedrals between the phenyls and hydantoin units. On the other hand, an almost quantitative agreement is observed between the calculated distances between the phenyl centroids and the two oxygens of the molecule in liquid phase and solid state.

The experimental UV-Vis and NMR spectra of DPH have been explained on the basis of the contributions due to Boltzmann weighted contributions of monomers and dimers. All the allowed electronic excitations are dominantly driven by charge-transfer type transitions between the subunits of the molecule.

The ^{1}H and ^{13}C NMR chemical shifts of DPH in DMSO were explained by considering the Boltzmann population averaged DFT calculated data for the six dimers. The only observed discrepancy between the experimental and computed data can be explained by the lack of describing the specific solute – solvent interactions.

The experimental Raman spectrum was obtained with five excitation laser lines and the assignment was made based on the calculated spectrum of a cluster of five DPH molecules. For this purpose we used the QM:QM methodology (two layers, B3LYP/3-21G level of theory for the low layer composed of 4 molecules and B3LYP/6-311+G(2d,p) for the high layer composed of one molecule. This methodology was found to be much more convenient compared to the anharmonic calculations, due to the much shorter time required for running the jobs.

The Raman bands in the spectrum recorded with the 325 nm laser are more enhanced with respect to the other lasers for Raman shifts greater than 800 cm^{-1}. For smaller wavenumbers, the 785 laser gives the most intense Raman bands. Pre-resonant conditions and the polarizability dependence of the molecule on the used laser could explain such behavior.

Chapter 5
CONFORMATIONAL LANDSCAPE AND LOW LYING EXCITED STATES OF IMATINIB

5.1 Introduction

Imatinib, (IMT, see Fig. 5.1), is a first generation tyrosine-kinase inhibitor (TKI), used mainly in the treatment of chronic myelogenous leukemia and gastrointestinal stromal tumors [Mul09, Ksi11, Had14]. It acts selectively on Abl tyrosine kinases [Sch09, Zha09, Zha10], Mast/stem cell growth factor receptor (c-Kit) and platelet-derived growth factor receptors (PDGF-R) [Rub02, Mak02].

The accurate description of the 3D arrangement and molecular properties of thermally accessible conformational states is crucial for understanding its interaction with receptors [Ale10, Che11, Lop12, Pis14].

Surprisingly, in spite of the importance of conformational space, to the best of our knowledge, only scarce data related to the conformers of IMT have been reported in the literature [Muc11, Che11]. For this reason, besides the conformational landscape, another interest was to compare the 3D structure of the bioactive conformations found in different IMT-tyrosine kinases complexes [Sch09, Zha09, Xio08, Che11] to that of other possible conformers.

5.2 Experimental and computational details

UV-Vis spectra of IMT in water were recorded using a Jasco V-670 UV–Vis–NIR spectrophotometer with a slit width of 2 nm, in a quartz cuvette of 1 cm path length.

The conformational space of IMT was explored initially with Tinker software, using the MMFF94 molecular mechanics force field [Shi13]. This way, 4,024 conformations were identified, within an energy window of 34 kcal·mol^{-1}.

For the next part of the study we used the hybrid B3LYP exchange-correlation functional [Bec93, Lee88, Vos80, Ste94] in conjunction with Pople's "spectroscopic" 6-31G(d) (BS1) and 6-31+G(d,p) (BS2) basis sets. Besides the first most stable 45 conformers, whose relative free energies are less than 3.5 kcal·mol^{-1} we also optimized the geometries of IMT conformers found in the two known polymorphic forms and in c-Abl kinase complexes, using their solid state structures as starting geometries. A total number of 49 conformers were optimized, whose relative energy spans a free energy interval from 0 to 4.80 kcal·mol^{-1}. Finally, the gas-phase structures were re-optimized in

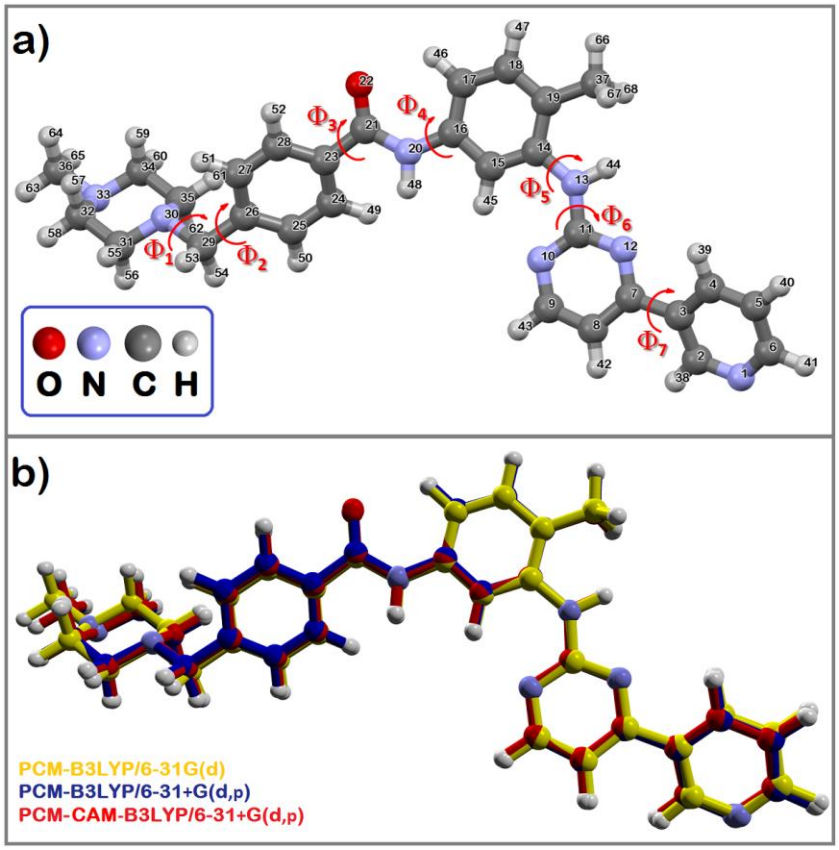

Fig. 5.1 a) Optimized structures of the most stable conformer of imatinib (IMT) in water **(5)** at (PCM)-B3LYP/6-31+G(d,p) level of theory; b) Superimposed optimized structures of the most stable conformer of IMT in water (5) at three levels of theory.

water at B3LYP/BS1 and B3LYP/BS2 levels of theory, using the PCM continuum solvation model [Tom05]. Fig. 5.2 present the first 9 most stable conformers, whose relative energies are less than the room temperature energy (0.592 kcal·mol^{-1}). For comparison purposes we also included the two optimized and experimental structures of the conformers found in c-Abl kinase complex and in the α and β polymorphs.

Absorption spectra of IMT were calculated using the CAM-B3LYP functional [Yan04] coupled to the 6-31+G(d,p) basis set and the simulated UV-Vis spectrum has been obtained by summation of the contributions from transitions to the first 80 singlet excited electronic states.

5.3 Conformational landscape of Imatinib

The most visible difference between C and T type conformers can be observed between those containing these letters in the sixth doublet, i.e, differing in the rotation around the N13-C14 bond.

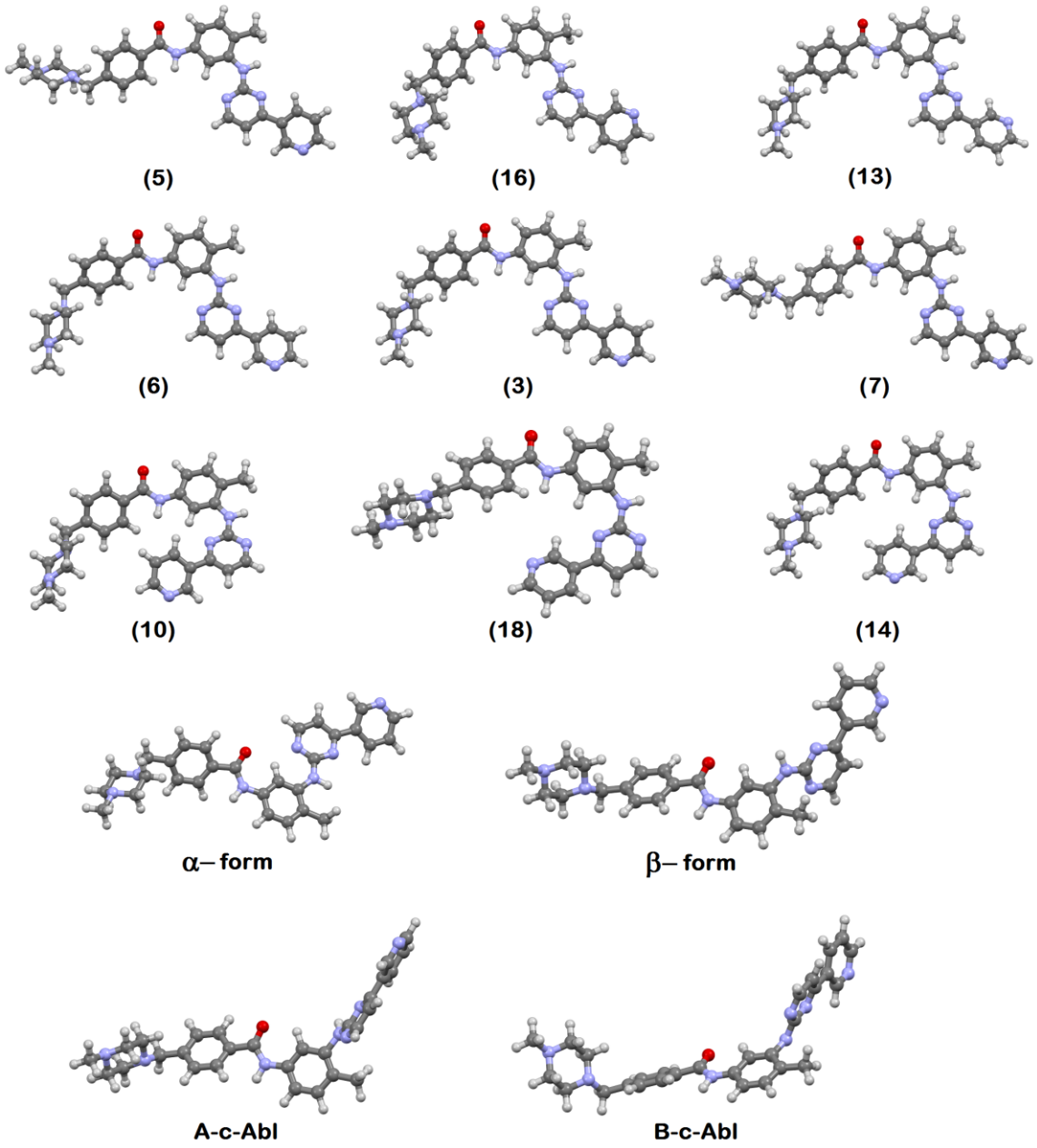

Fig. 5.2 PCM-B3LYP/6-31+G(d,p) optimized structures of the nine most stable IMT conformers in water, together with α and β crystal forms [Gri13], as well as with the A and B-forms found in the kinase complex of c-Abl [Nag02]. (reproduced from ref. [Vin15])

The conformers with the sixth doublet as C- and C+ have a V-shape, [Nag02], while the conformers having the sixth doublet T- and T+ are U-shaped (see Fig. 5.2). It is worth mentioning note that only the conformer (15) (see Table 5.4) has an S-like shape, closest to that of the α and β polymorphs and to the structures found in IMT-c-Abl complexes. Special attention has been paid to the piperazine fragment of IMT. In the chair form of N,N'-dimethyl-piperazine, which, according to our calculations, is more

stable than the skewed boat by 8.23 kcal·mol^{-1}, the two N-CH_3 bonds can remain equatorial or axial, leading to three different conformations, eq-eq, eq-ax and ax-ax, with relative Gibbs energy of 0.00, 6.47 and 7.69 kcal·mol^{-1}, respectively.

The most stable conformer in gas-phase (1) has the piperazine fragment in the chair form with eq-eq conformation. According to data presented in Fig. 5.2, the chair conformation is preserved for all IMT conformers considered within a relative Gibbs energy of 0.49 kcal·mol-1.

As shown in Table 5.2, the first nine most stable conformers in water are dominant, constituting more than 68% Boltzmann population. The most stable conformer in gas-phase is **(1)**, while conformer **(5)** is the most stabilized in water; the main differences between the structures of the two conformers consist in the relative orientation of the piperazine group relative to the rest of the molecule. Such difference is expected considering that this group represents the hydrophobic moiety of IMT [Nag02]. The α dihedral angle between the pyridine and methylbenzene rings has values between 50^o and 90^o in type II inhibitor-protein complexes, but for the first most stable nine free IMT conformers in Table 5.1, α values oscillate between -35^o ÷ 32^o. The β dihedral angle between piperazine and methylbenzene group is largely distributed between 0^o and 90^o in protein-imatinib complexes and the same happens for the free conformers whose β values are between 42^o and 77^o.

Table 5.4 lists the experimental dihedral angles of IMT as found in the c-Abl kinase complex [Nag02], but also the α and β polymorphic forms [Gri13]. The dihedral angle Φ_5 for IMT in tyrosine kinase complex is 97.5^o giving rise to a value of 92.6^o for α angle, characteristic for type II inhibitors.

Notably, only conformer (15) has a S-like shape, resembling the conformation found in both, solid state polymorphs [Gri13] and c-Abl-IMT complex [Nag02]. Moreover, from Fig. 5.2 it is evident that the major difference between the structures of the free V-shape conformers and the bioactive conformer bound to c-Abl kinase consists in the relative orientation of the pyrimidine-pyridine groups. It is this moiety through which the IMT ligand binds to the ATP pocket of TK.

To conclude the discussion about the structural features of IMT conformers, we would like to note that the BS1 basis set was demonstrated as a good compromise for obtaining optimized geometries, relative energies and even excitation energies, at least for small or medium-sized molecules [Jua13, Per13, Sur14, Chi14, Sjo14].

Table 5.2 Relative free energies and Boltzmann populations of the 20 most stable conformers of imatinib in gas-phase [B3LYP/6-31G(d) level of theory] and in water [PCM-B3LYP/6-31G(d) and PCM-B3LYP/6-31+G(d,p) levels of theory] at room temperature

Conformer	Gas-phase B3LYP/6-31G(d)		Water PCM-B3LYP/6-31G(d)		Water PCM-B3LYP/6-31+G(d,p)	
	ΔG[a] (kcal·mol^{-1})	Population (%)	ΔG[b] (kcal·mol^{-1})	Population (%)	ΔG[c] (kcal·mol^{-1})	Population (%)
G-A+C-C-C+C-T- **(1)**	0.00	16.24	0.31	6.15	1.06	1.85
G-A+C-C-C+C+T- **(2)**	0.40	8.38	0.35	5.75	1.07	1.83
T-G+C-C-C-C-T- **(3)**	0.40	8.37	0.26	6.64	0.27	7.07
G-A+C-C-C+C-T+ **(4)**	0.44	7.82	0.14	8.12	0.66	3.67
T-A-C-C-C-C+T- **(5)**	0.48	7.28	0.00	10.33	0.00	11.13
T-G+C-C-C+C+T+ **(6)**	0.69	5.16	0.35	5.74	0.26	7.22
G-A+C+C+C+C-T- **(7)**	0.71	4.95	0.51	4.38	0.34	6.29
G-G-C-C-C+C+T- **(8)**	0.72	4.84	0.85	2.49	0.65	3.72
T-G+C+C+C-C+T- **(9)**	0.74	4.72	0.83	2.58	0.94	2.28
T-G+C-C-C-T+T+ **(10)**	0.97	3.22	0.16	7.86	0.41	5.57
G-A+C-C-C+C-C- **(11)**	0.97	3.20	0.29	6.31	0.63	3.87
T-G+C+C+C+T-T- **(12)**	0.97	3.19	1.18	1.45	0.78	3.00
T-G+C+C+C-C+C- **(13)**	1.02	2.97	0.42	5.14	0.03	10.59
T-G+C-C-C+T-T- **(14)**	1.04	2.87	0.47	4.73	0.49	4.84
T-G+C-T+C-T+T- **(15)**	1.04	2.84	1.12	1.59	1.69	0.64
T-G+C+C+C-C+C+ **(16)**	1.05	2.83	0.15	8.07	0.03	10.63
G-A+C-C-C+C-C+ **(17)**	1.05	2.81	0.43	5.05	1.09	1.76
T-G+C-C+C+T-T- **(18)**	1.05	2.79	0.48	4.66	0.49	4.86
T-A-C+C-C-T-C+ **(19)**	1.06	2.77	1.13	1.56	0.98	2.13
G-A+C-C-C+T-T- **(20)**	1.06	2.76	1.20	1.38	0.72	3.30

[a]relative to conformer **(1)**
[b]relative to conformer **(5)**
[c]relative to conformer **(5)**

On the other hand, the basis set drastically affects the relative stability of the conformers. It is possible to estimate the difference in fusion enthalpies between two polymorphic forms as the difference between the enthalpies of conformers in gas-phase [Pol01, Kla00].

Table 5.4 Experimental and calculated dihedral angles (degrees) and relative free energy characterizing the IMT α and β crystal forms [Dic09] and A-form and B-form in tyrosine kinase complex [Ste94] and their optimized conformers in water. *Exp*. Experimental data, *Opt*. Optimized; A, B. The two forms found in c-Abl kinase complexes with IMT [Ste94]; α, β the two structures determined in the α and β polymorphs of imatinib [Che11]

	ΔG[a)]	**Φ1**	**Φ2**	**Φ3**	**Φ4**	**Φ/5**	**Φ6**	**Φ7**
Exp. A [Nag02]	n.a.	-179.0	49.4	15.7	-176.6	97.5	-0.5	170.3
Opt.-A water	1.77	-166.6	46.0	27.3	-175.4	112.8	5.3	156.6
Exp. B [Nag02]	n.a.	-179.8	49.4	24.6	-179.8	97.5	-0.5	-12.1
Opt.-B water	1.60	-168.0	53.4	27.6	-176.3	112.3	5.4	-23.7
Exp. α [Gri13]	n.a.	-165.7	43.5	-25.8	-164.6	77.9	-26.9	36.6
Opt. α water	1.19	-167.7	48.8	-29.2	-168.7	-6.1	-0.8	24.4
Exp. β [Gri13]	n.a.	-168.3	23.7	35.3	-129.2	-113.3	-3.9	-13.2
Opt. β water	1.47	-167.5	52.2	27.8	-0.6	-111.0	-6.8	-24.1

[a)] relative to conformer **(5)**

Exp. - experimental data; Opt.-optimized; A, B – the two forms found in c-Abl kinase complexes with imatinib [Nag02]; α, β - the two structures determined in the α and β polymorphs of imatinib [Gri13]; n.a. – not available

Thus, for an ideal solution, the mole fraction x of solute at saturation is a function of fusion enthalpy ΔH, molar heat capacity ΔC_p, the melting temperature T_m and the temperature T of the solution [Pol01]:

$$x = exp(-(\Delta H/R)\cdot(\frac{1}{T}-\frac{1}{T_m}) + (\Delta C_p/R)\cdot((T_m - T)/T + ln(T/T_m)) \quad (5.1)$$

For IMT, the difference in fusion enthalpy is estimated as H_β-H_α = 2.45 kJ·mol^{-1} and the difference in molar heat capacity ΔC_p is approximated by the difference in fusion entropy (ΔS_β-ΔS_α = -3.67 JK^{-1}mol^{-1}) for transition from crystal form to supercooled liquid form (as $\Delta S = S_{gas}$-S_{water}). The ratio x_α/x_β was calculated as:

$$x_\alpha/x_\beta = exp\left(\frac{H_\beta - H_\alpha}{R}\cdot\left(\frac{1}{T}-\frac{1}{T_{mm}}\right) - \frac{\Delta S_\beta - \Delta S_\alpha}{R}\cdot\left(\frac{T_m - T}{T} + ln\left(\frac{T}{T_{mm}}\right)\right)\right) \quad (5.2)$$

where T_{mm} = 494.5 K is the average value of the experimental melting temperatures of the two polymorphs [Gri13]. At room temperature (T=298 K) we obtained a value of 2.26 for the ratio of mole fractions, in excellent agreement with experimental finding that α-form polymorph is 2.5 times more soluble than the β-form.

In addition, considering the difference in experimental fusion enthalpies between β and α forms of 3.18 kJ·mol^{-1} [Gri13] our calculations predict that 2.45 kJ·mol^{-1} is due to conformational difference and 0.73 kJ·mol^{-1} is due to the difference of the Van der Waals interactions in crystal.

5.4 Electronic transitions and UV-Vis spectrum of Imatinib

Figure 5.4 illustrates the evolution of the UV-Vis spectrum of IMT in water as a function of concentration within the 10^{-5}-10^{-4} M range. While a clear red-shift of the

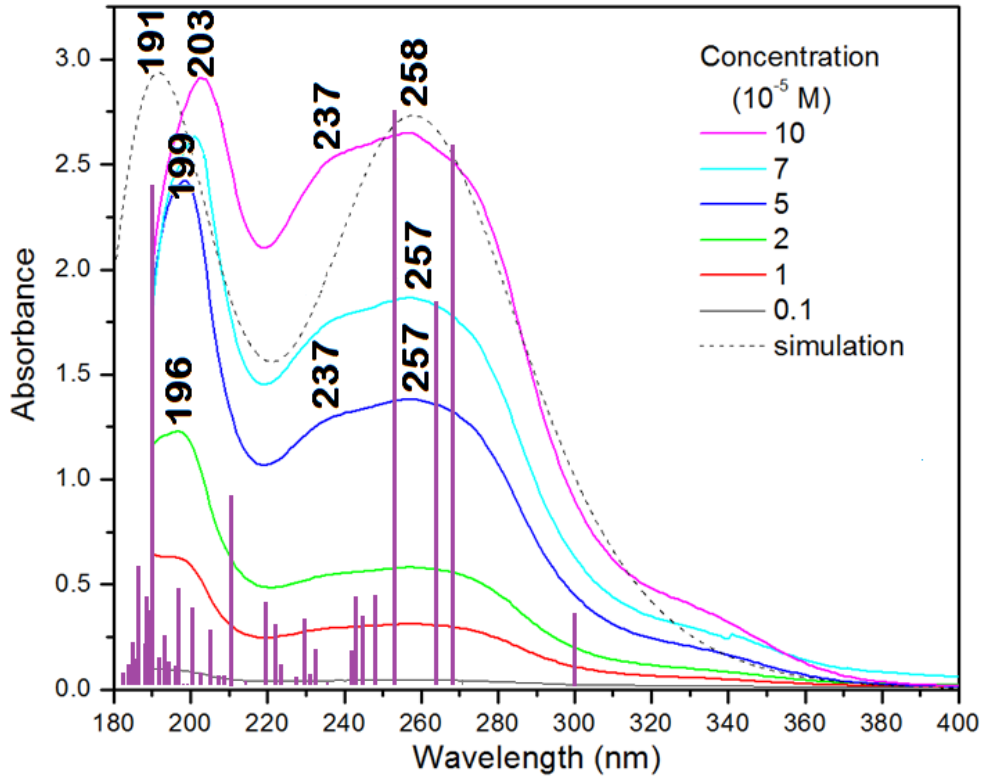

Fig. 5.4 Concentration dependence of the absorption spectra of IMT in water at room temperature. The simulated spectrum was calculated as Boltzmann population averaged spectra at room temperature of the nine most stable conformers in water. The *stick spectrum* corresponds to conformer **(5)**.

peak around 195-203 nm is observed by increasing the concentration, the other two absorbance peaks at 237 nm and 257 nm do not change their positions.

The UV-Vis spectrum of IMT was calculated at CAM-B3LYP/BS2//B3LYP/BS2 level of theory. For concentrations lower than 10^{-4} M it is assumed that the monomers contribute predominantly to the absorption spectrum in solution. The relative Gibbs energies (ΔG) and populations given in Table 5.2 suggest that the predominant contribution to UV-Vis spectra of IMT in water comes from the nine most stable imatinib monomers **(5), (16), (13), (6), (3), (7), (10), (18)** and **(14)** whose relative energies are within 0.49 kcal·mol^{-1} and together constitute more than 68% of the total

population.-As shown in Fig. 5.4, the positions and intensities of the experimental bands are very well reproduced by calculations.

According to quantum chemical calculations, each of the nine most stable conformers of IMT give mainly four calculated absorption bands: around 190 nm, due mainly to HOMO-6→LUMO+4 transition; at 254 nm, due to HOMO-2→LUMO+1 transition; at 265 nm, due to HOMO→LUMO+1 transition and 270 nm due to HOMO→LUMO+1 and HOMO→LUMO+2 transitions.

The analysis of the shapes of MOs involved in the above mentioned transitions of **(5)** in water show that the highest energy observed transition (HOMO-6→LUMO+4) at 190 nm is mainly due to a redistribution of electronic charge onto the phenyl moiety. The electronic transition HOMO-2→LUMO+1 at 254 nm is a result of charge transfer from methylbenzene and piperazine rings to phenyl group, concomitant with a redistribution of charge within the methylbenzene ring. The HOMO orbital is delocalized onto the methylbenzene, pyrimidine and amide group. The lowest energy electronic transitions HOMO→ LUMO+1 and HOMO-LUMO+2 simulated in water at 258 nm and observed experimentally at 257 nm is due to the charge transfer from methylbenzene and pyrimidine groups to the phenyl ring.

5.5 Conclusions

Combining molecular mechanics and DFT quantum chemistry methods we were able to characterize 20 conformers of IMT, all of them being confirmed as minima on the PES. The relative Gibbs energies of the nine most stable IMT monomers in water were within 0.49 kcal·mol^{-1} and together constitute more than 68% of the total population.

In water solution, IMT presents three UV-Vis absorbance peaks in the range 195-203 nm, 237 nm and 257 nm. A reliable assignment of the electronic transitions of IMT is provided based on the Boltzmann populations-averaged spectra of its conformers in water. While 6-31G(d) basis set seems to be an optimum choice for geometry optimizations of IMT and presumably, for similar drugs, the 6-31+G(d,p) is required for relative energies and excitation energy calculations. Only by using the CAM-B3LYP long range corrected functional was it possible to reproduce quantitatively the lowest energy electronic absorption peak. Based on the calculated thermochemical data, a value of 2.26 was estimated for the ratio of mole fractions x_α/x_β corresponding to the two known polymorphs of IMT, in excellent agreement with previously published experimental findings.

References

[Ada99] C. Adamo, V. Barone, *J. Chem. Phys.,* 110 (1999) 6158-6169.

[Ale10] A. Aleksandrov, T. Simonson, J. Comput. Chem., 31 (2010) 1550-1560.

[APFD] A. Austin, G. Petersson, M. J. Frisch, F. J. Dobek, G. Scalmani, and K. Throssell*, J. Chem. Theory and Comput.*, 8 (2012) 4989-5007.

[Ati16] M. Atif, M. Azeem, M. Rehan Sarwar, SpringerPlus, 5 (2016) 182.

[Bal82] U. Balachandran, N. G. Eror, *J. Solid State Chem.,* 42 (1982) 276-282.

[Bar14] V. Barone, M. Biczysko, J. Bloino, *Phys. Chem. Chem. Phys.* 16 (2014) 1759-1787.

[Bar15] V. Barone, E. Benassi, I. Carnimeo, in J.L. Rivail, M. Ruiz-Lopez, X. Assfeld X., *Quantum Modeling of Complex Molecular Systems. Challenges and Advances in Computational Chemistry and Physics*, vol 21, 2015, Springer, Cham.

[Bec93] A.D. Becke, *J. Chem. Phys.,* 98 (1993) 5648-5652.

[Bia10] M. Bialer, K.K. Midha, Epilepsia, 51 (2010) 941–950.

[Biorad] Bio-Rad Laboratories, Inc. SpectraBase; SpectraBase Compound ID=UhBVhrEdKp http://spectrabase.com/compound/UhBVhrEdKp (accessed Jul 21, 2017).

[Bor09] M. Bortolotti, L. Lutterotti and I. Lonardelli, J. Appl. Cryst., 42 (2009) 538-539.

[Buc17] K. Buckley, A.G. Ryder, *Appl. Spectrosc.,* 71 (2017) 1085-1116.

[Cam71] A. Camerman, N. Camerman, *Acta Cryst. B27* (1971) 2205.

[Car03] M. Carter, V. Stephenson, D. Weaver, *J. Mol. Struct. (Theochem),* 638 (2003**)** 57-62.

[Cas98] M. E. Casida, C. Jamorski, K. C. Casida, D. R. Salahub, J. Chem. Phys., 108 (1998) 4439-4449.

[Che11] I.-J. Chen, N. Foloppe, *Drug. Dev. Res.*, 72 (2011) 85-94.

[Chi14] S. Chibani, D. Jacquemin, A.D. Laurent, *Comput. Theor. Chem.*, 1040–1041 (2014) 321–327

[Chu15] L. W. Chung, W. M. C. Sameera, R. Ramozzi, A. J. Page, M. Hatanaka, G. P. Petrova, T. V. Harris, X. Li, Z. Ke, F. Liu, H.-B. Li, L. Ding, K. Morokuma, *Chem. Rev*., 115 (2015) 5678–5796.

[Cla06] A.E. Clark, *J. Phys. Chem.* A 110 (2006) 3790-3796.

[Cor16] Y. Cornaton, M. Ringholm, O. Louant, K. Ruud, *Phys. Chem. Chem. Phys*., 18 (2016) 4201-4215.

[Cou03] R. Coupez, R. Straetemans, G. Sehgal, A. Stockis, Z.S. Lu, *J. Clin. Pharm*. 43 (2003) 1370–1376.

[Dat04] S. Datta, D.J.W Grant, *Nat. Rev. Drug Disc.,* 3 (2004) 42-57.

[Deg14] K. Dégardin, Y. Roggo, P. Margot, *J. Pharm. Biomed. Anal.,* 87 (2014) 167– 175.

[Dic09] Diculescu VC, Chiorcea-Paquima A-M, Tugulea L, Vivan M, Oliveira-Brett A-M, *Bioelectrochemistry*, 74 (2009)278–288.

[Dit74] R. Ditchfield, *Mol. Phys.* 27 (1974) 789-807.

[Duc07] L. Ducasse, F. Castet, A. Fritsch, I. Huc and T. Buffeteau, *J. Phys. Chem. A*, 111 (2007) 5092-5098.

[Eti14] T. Etienne, C. Michaux, A. Monari, X. Assfeld, E.A. Perpète, *Dyes Pigm.,* 100 (2014) 24-31.

[Far09] M.U. Farooq, A. Bhatt, A. Majid, R. Gupta, A. Khasnis, M.Y. Kassab, *Am. J. Health-Syst. Pharm.,* 66 (2009) 541–561.

[Fri84] M.J. Frisch, J.A. Pople and J.S. Binkley, *J. Chem. Phys.,* 80 (1984) 3265-3269.

[Gau09] Gaussian 09, Revision C.01, M. J. Frisch, G. W. Trucks, H. B. Schlegel, G. E. Scuseria, M. A. Robb, J. R. Cheeseman, G. Scalmani, V. Barone, B. Mennucci, G. A. Petersson, H. Nakatsuji, M. Caricato, X. Li, H. P. Hratchian, A. F. Izmaylov, J. Bloino, G. Zheng, J. L. Sonnenberg, M. Hada, M. Ehara, K. Toyota, R. Fukuda, J. Hasegawa, M. Ishida, T. Nakajima, Y. Honda, O. Kitao, H. Nakai, T. Vreven, J. A. Montgomery, Jr., J. E. Peralta, F. Ogliaro, M. Bearpark, J. J. Heyd, E. Brothers, K. N. Kudin, V. N. Staroverov, T. Keith, R. Kobayashi, J. Normand, K. Raghavachari, A. Rendell, J. C. Burant, S. S. Iyengar, J. Tomasi, M. Cossi, N. Rega, J. M. Millam, M. Klene, J. E. Knox, J. B. Cross, V. Bakken, C. Adamo, J. Jaramillo, R. Gomperts, R. E. Stratmann, O. Yazyev, A. J. Austin, R. Cammi, C. Pomelli, J. W. Ochterski, R. L. Martin, K. Morokuma, V. G. Zakrzewski, G. A. Voth, P. Salvador, J. J. Dannenberg, S. Dapprich, A. D. Daniels, O. Farkas, J. B. Foresman, J. V. Ortiz, J. Cioslowski, and D. J. Fox, Gaussian, Inc., Wallingford CT, 2010.

[Geo14] F. George, N. Tumanov, B. Norberg, K. Robeyns, Y. Filinchuk, J. Wouters, T. Leyssens, *Cryst. Growth Des.,* 14 (2014) 2880-2892.

[Gog01] T.M. El-Gogary, M.S Soliman, *Spectrochim. Acta A*, 57 (2001) 2647 – 2657.

[Gri13] Grillo D, Polla G, Vega D, *J. Pharm. Sci*., 101 (2013) 541–551.

[Gua02] F. Gualtieri, D. Manetti, M.N. Romanelli, C. Ghelardini, *Curr. Pharm. Des*., 8 (2002) 125–138.

[Had14] Al-Hadiya BMH, Bakheit AHH, Abd-Elgalil AA, Profiles of Drug Substances, Excipients and Related Methodology, Chapter Six - Imatinib Mesylate, 39 (2014) 265-298.

[Hal15] A. Halasa, L. Lapinski, I. Reva, H. Rostkowska, R. Fausto and M. J. Nowak, *J. Phys. Chem. A,* 119 (2015) 1037–1047.

[Hed13] A. Hédoux, Y. Guinet, L. Paccou, F. Danède, P. Derollez, *J. Pharm. Sci*., 102 (2013) 162-170.

[Heh72] W.J. Hehre, R. Ditchfield, J.A. Pople, *J. Chem. Phys.,* 56 (1972) 2257-2261.
[Her13] C. Herman, V. Vermylen, B. Norberg, J. Wouters and T. Leyssens, *Acta Cryst.* B69 (2013), 371-378.
[Hig17] K. Higashi, K. Ueda, K. Moribe, *Adv. Drug. Delivery Rev.,* 117 (2017) 71-85.
[Hoh64] P. Hohenberg, W. Kohn, *Phys. Rev.,* 136 (1964) B864.
[Hon71] B. Honig, M. Karplus, *Nature*, 229 (1971) 558-560.
[Hum96] S. Humbel, S. Sieber, K. Morokuma, *J. Chem. Phys*., 105 (1996) 1959-1967.
[Ict15] E. Içten, A. Giridhar, Z. K. Nagy, G. V. Reklaitis, *AAPS Pharm. Sci. Tech.,* 17 (2015) 284-293.
[Ild12] G.O. Ildiz, I.Boz, O. Unsalan, *J. Optics and Spectroscopy,* 112 (2012) 665-670
[Jes15] A.J. Lopes Jesus, S. Jarmelo, R. Fausto and I. Reva, *Spectrochim. Acta A*, 140 (2015) 54–64.
[Jua13] Juaristi E, Notario R, *Struct. Chem.,* 24 (2013) 1855-1862.
[Kha90] Y.D. Khamchukov, S.N. Shashkov, I.V. Lukomskii, J. Appl. Spectrosc. 53 (1990) 1281–1286.
[Kim03] T. Kimura and Y. Nagao, Bull. *Fac. Sci. Tech. Hirosaki Univ.* 5, 11 (2003).
[Kin11] M.D. King, W.D. Buchanan, T.M. Korter, *J. Pharm. Sci.,* 100 (2011) 1116-1129.
[Kla00] Klamt A, Eckert F, *Fluid. Phase Equilibr*., 172 (2000) 43-72.
[Kli16] H. Klitgaard, A. Matagne, J.M. Nicolas, M. Gillard, Y. Lamberty, M. De Ryck, R.M. Kaminski, K. Leclercq, I. Niespodziany, C. Wolff, M. Wood, J. Hannestad, S. Kervyn, B. Kenda., *Epilepsia*, 57 (2016) 538-48.
[Kra07] G. Krämer, A. Biraben, M. Carreno, A. Guekht, G.J.de Haan, J. Jedrzejczak, D. Josephs, K. van Rijckevorsel, G. Zaccara G, *Epilepsy Behav*., 11 (2007) 46-52.
[KS65] W. Kohn, L. J. Sham, *Phys. Rev.,* 140 (1965) A1133.
[Kse10] D.N. Ksenafontov, N.F. Moiseeva, L.V. Khristenko, N.M. Karasev, I.F. Shishkov, L.V. Vilkov, *J. Mol. Struc*., 984 (2010) 89–95.
[Ksi11] D. Ksienski, Clin. Med. *Insights Oncol.,* 5 (2011) 365–379.
[Lac12] F. Lachaud, C. Jeandon, M. Beley, R. Ruppert, P.C. Gros, A. Monari and X. Assfeld, *J. Phys. Chem. A* 116 (2012) 10736−10744.
[Lap01] A Łapiński, J. Spanget-Larsen, M. Langgård, J. Waluk, J. G. Radziszewski, *J. Phys. Chem. A*, 105 (2001) 10520–10524.
[Lee88] C. Lee, W. Yang, R.G. Parr, *Phys. Rev. B,* 37 (1988) 785.
[Li11] L. Li, Y.-K. Si, *J. Pharm. Biomed. Anal.,* 56 (2011) 465–470.
[Lin91] D. Lin-Vien, N.B. Colthup, W.G. Fateley, J.G. Grasselli, *The Handbook of Infrared and Raman Characteristic Frequencies of Organic Molecules*, Academic Press, 1991.
[Lop11] F.Lopez-Vallejo, M. Fragoso-Serrano, G. A. Suarez-Ortiz, A.C. Hernandez-Rojas, C.M. Cerda-García-Rojas, R. Pereda-Miranda, *J. Org. Chem*., 76 (2011) 6057–6066.
[Luc14] **R. Luchian**, R.-A. Domokos, C. Chiş, M. Vasilescu, E. Vinţeler, V. Chiş, *Studia UBB Physica*, 59 (LIX), 2 (2014) 85-98.
[Luc15] **R. Luchian**, E. Vinţeler, C. Chiş, M. Vasilescu, N. Leopold, V. Chiş, *Croat. Chem. Acta*, 88 (2015) 511–522.
[Luc17] **R. Luchian**, E. Vinţeler, C. Chiş, M. Vasilescu, N. Leopold 1, J.P. Prates Ramalho, V. Chiş, *J. Pharm Sci.,* 106 (2017) 3564-3573.
[Mak02] Maki RG, Awan RA, Dixon RH, Jhanwar S, Antonescu CR, *Int. J. Cancer*, 100 (2002) 623–626.
[Mar03] R.L. Martin, *J. Chem. Phys.* 118 (2003) 4775-4777.
[Mar15] S. Marković and J. Tošović, *J. Phys. Chem. A* 119 (2015) 9352-9362.
[Mat02] A.E. Mattsson, *Science*, 298 (2002) 759-760.
[Muc11] Mucs D, Bryce RA, Bonnet P, *J. Comput. Aid Mol. Des*., 25 (2011) 569-581.
[Mul09] Muller BA, *Curr. Pharm. Des*., 15 (2009) 120-133.
[Nag02] N. Naga, Master Thesis, *An investigation into the possible neuroprotective properties of phenytoin*, Rhodes University 2002.
[Nag02b] Nagar B, Bornmann W, Pellicena P, Schindler T, Veach DR, Miller WT, Clarkson B, Kuriyan J, *Cancer. Res.,* 62 (2002) 4236-4243.
[Ner16] N. Nergui, M.–J. Chen, J.-K. Wang, Y.-L. Wang, C.-R. Hsing, C.-M. Wei, Kaito Takahashi, *J. Phys. Chem. A*, 120 (2016) 8114−8122.
[Ohs80] T. Ohsaka, *J. Phys. Soc. Jpn*., 48 (1980) 1661-1668.
[Ora15] V. Oral, S.Ç, Andaç, *J. Pharm. Istanbul Univ*., 45 (2015) 253-266.
[Par04] R.B. Parthasaradhi, R.K. Rathnakar, R.R. Raji, R.D. Muralidhara, C.R.K. Subash, "*Novel crystalline forms of levetiracetam*", Patent WO2004083180 A1, September 30, 2004.
[Per13] Perrier A, Maurel F, Browne WR, Jacquemin D, *Chem. Comm*., 49 (2013) 4247-4249.
[Per96] J. P. Perdew, K. Burke, M. Ernzerhof, *Phys. Rev. Lett.,* 77 (1996) 3865.
[Per97] J. P. Perdew, K. Burke, M. Ernzerhof, *Phys. Rev. Lett.,* 78 (1997) 1396.

[Pic15] M. Piccardo, J. Bloino, V. Barone, *Int. J. Quantum Chem*., 115 (2015) 948–982.
[Pin17] E. Pindelska., A. Sokal., W. Kolodziejski, *Adv. Drug Delivery Rev*., 117 (2017) 111-146.
[Pis14] P. Pisani, P. Piro, S. Decherchi, G. Bottegoni, D. Sona, V. Murino, W. Rocchia, A. Cavalli, *J. Chem. Theory Comput*., 10 (2014) 2557–2568.
[Pit05] A. Pitkanen, *Epilepsy Curr.,* 5 (2005) 14-16.
[Pol01] Poling BE, Prausnitz JM, O'Connell JP (2001) *The Properties of Gases and Liquids*, McGraw-Hill, New York
[Ren14] S. Renuga, S. Muthu , *Spectrochim. Acta A*, 118 (2014) 702–715.
[Rub02] Rubin BP, Schuetze SM, Eary JF, Norwood TH, Mirza S, Conrad EU, Bruckner JD*, J. Clin. Oncol.*, 20 (2002) 3586–3591.
[Sca10] G. Scalmani and M.J. Frisch, *J. Chem. Phys.* 132 (2010) 114110.
[Sch09] Schindler T, Bornmann W, Pellicena P, Miller WT, Clarkson B, Kuriyan J, *Science*, 289 (2009) 1938–1942.
[Shi13] Y. Shi, Z. Xia, J. Zhang, R. Best, C. Wu, J. W. Ponder, P. Ren, *J. Chem. Theory Comput*., 9 (2013) 4046-4063.
[Sjö14] J. Sjöqvist, R.C. González-Cano, J.T. López Navarrete, J. Casado, M.C. Ruiz Delgado, M. Linares, P. Norman, *Phys. Chem. Cjem. Phys*., 16 (2014) 24841-24852.
[Son03] J. Song, K.X. Lou, X.J. Li, X.P. Wu, R.X. Feng, *Acta Cryst.* E59 (2003) 1772-1773.
[Son11] H.H. Sonmezturk, N.J. Azar, *J. Cent. Nerv. Syst. Dis.,* 3 (2011) 17-25.
[Sou07] S.F. Sousa, P. Fernandes, and M. Joao Ramos, *J. Phys. Chem. A,* 111 (2007) 10439-10452.
[Ste94] P.J. Stephens, F.J. Devlin, C.F. Chabalowski, M.J. Frisch, *J. Phys. Chem.,* 98 (1994) 11623-11627.
[Sur14] Suresh Kumar NV, Singh H, *J. Phys. Chem. A*, 118 (2014) 2120-2137.
[Tha09] R.K. Thaper, M.D. Prabhavat, *A novel polymorph of levetiracetam and a process for its preparation*, Patent WO2009050735A1, April 23, 2009.
[Tho06] F.C. Thorley, K.J. Baldwin, D.C. Lee, D.N. Batchelder, *J. Raman., Spectrosc*., 37 (2006) 335-341.
[Tie08] K.E. Tiedje and D.F. Weaver, *Can. J. Neurol. Sci.,* 35 (2008) 232-236.
[Tom05] J. Tomasi, B. Mennucci, R. Cammi, *Chem. Rev.,* 105 (2005) 2999-3093.
[Ull09] C.M. Ulla, A.Towfigh, J. Safdieh, Neuropsichtr. *Dis. treat.,* 5 (2009) 467-476.
[Vai15] S. Vaithianathan, S. Raman, W. Jiang, T.Y. Ting, M.A. Kane, J.E. Polli,, *Mol. Pharmaceutics.*, 12 (2015) 2436–2443.
[Vei09] M. de Veij, P. Vandenabeele, T. De Beer, J.P. Remon, L. Moens, *J. Raman Spectrosc*., 40 (2009) 297–307.
[Vel14] G. Velmurugan, B. K. Ramamoorthi and P. Venuvanalingam, *Phys. Chem. Chem. Phys.,* 16 (2014) 21157-21171.
[Vin15] E. Vinţeler, N.-F. Stan, **R. Luchian**, C. Căinap, J.P. Prates-Ramalho, V. Chiş, *J. Mol. Model.*, 21 (2015) 84.
[Vos80] S.H. Vosko, L. Wilk, M. Nusair, *Can. J. Phys*., 58 (1980) 1200-1211.
[War72] A. Warshel, M. Karplus, *J. Am. Chem. Soc.*, 94 (1972) 5612; A. Warshel, M. Karplus, *J. Am. Chem. Soc.*, 96 (1974) 5677.
[War76] A. Warshel, M. Levitt, *J. Mol. Biol.*, 103 (1976) 227.
[Wil14] P.H. Willoughby, M.J. Jansma, T.R. Hoye, *Nat. Protoc.,* 9 (2014) 643–660.
[Wol90] K. Wolinski, J.F. Hilton, P. Pulay, *J. Am. Chem. Soc.,* 112 (1990) 8251-8260.
[Xio08] Y.Z. Xiong, P.-Y. Chen, *J. Mol. Model.,* 14 (2008) 1083-1086.
[Xu14] K.L. Xu, B. Liang, X.Q Wu, L.L. Zhang, P.X. Tang, H. Li, *Powder Diffraction*, 29 (2014) 51-52.
[Yan04] Yanai T, Tew D, Handy N, Chem. Phys. Lett., 393 (2004) 51-57.
[Zha09] Zhang J, Yang PL, Gray NS, *Nat. Rev. Cancer,* 9 (2009) 28-39.
[Zha10] Zhang J, Adrián FJ, Jahnke W, Cowan-Jacob SW, Li AG, Iacob RE, Sim T, Powers J, Dierks C, Sun F, Guo G-R, Ding Q, Okram B, Choi Y, Wojciechowski A, Deng X, Liu G, Fendrich G, Strauss A, Vajpai N, Grzesiek S, Tuntland T, Liu Y, Bursulaya B, Azam M, Manley PW, Engen JR, Daley GQ, Warmuth M, Gray NS, *Nature*, 463 (2010) 501-507.